

1 **Implications of Sea Breeze Circulations on Boundary Layer**
2 **Aerosols in the Southern Coastal Texas Region**

3 **Tamanna Subba¹, Michael P. Jensen¹, Min Deng¹, Scott E. Giangrande¹, Mark C.**
4 **Harvey², Ashish Singh¹, Die Wang¹, Maria Zawadowicz¹, Chongai Kuang¹**

5 ¹Environmental Science and Technologies, Brookhaven National Laboratory, Upton, NY,
6 United States

7 ²Department of Physics, Texas Southern University, Houston, TX, United States

8 **Correspondence:** Tamanna Subba (tsubba@bnl.gov)

9
10 **Abstract**

11 The Sea Breeze Circulation (SBC) influences atmospheric processes at multiple scales in
12 coastal regions. Understanding how SBCs impact the aerosol number budget and aerosol-cloud
13 interaction processes is essential. This study investigates sea breeze–aerosol interactions
14 (SAIs) during 46 summertime SBC events using data from the TRacking Aerosol Convection
15 Interactions Experiment (TRACER) field campaign across urban (main) and rural
16 (supplemental) coastal sites in southern Texas. Weather Research and Forecasting model
17 coupled with Chemistry (WRF-Chem) simulations complement observations to explore spatio-
18 temporal meteorological controls on boundary layer aerosols. During the summertime, Sea
19 Breeze Fronts (SBF) penetrating inland transported cool, moist air over the land, introducing
20 air masses with distinct properties compared to the preexisting continental air. These SAIs
21 cause variability in number concentrations of up to a factor of two, with events typically lasting
22 ~5 hours before returning to background conditions. SAI impact on aerosols varies with site
23 proximity to water and the preceding sea breeze (SB) history, primarily affecting the marine-
24 influenced accumulation mode. The main site, influenced by both Galveston Bay and the Gulf
25 of Mexico, reflects a stronger marine influence. In contrast, a supplemental site, at a similar
26 shoreline distance but exposed only to the Gulf of Mexico and typically upstream of the urban
27 core, samples SB air that has traversed land and partially regained continental characteristics.
28 Simulations show that the regional SAIs extend ~50 km inland and reach up to the boundary
29 layer height. SAIs further decrease cloud condensation nuclei relevant aerosol number
30 concentrations in ~20% of events during SBF passage.

31 1 Introduction

32 A significant portion of the global population resides in coastal cities, including several
33 megacities (Brown et al., 2013). Nearly half of the U.S. population faces environmental
34 challenges associated with complexities tied to urban coastal atmospheres (Crossett et al.,
35 2004; Hudson et al., 2012). Houston, located along the Southern Texas coastline, is one of the
36 United States' most populated cities, while also one of its most polluted, with high aerosol
37 concentrations (Yoon et al., 1994; Kleinman et al., 2002; Banta et al., 2011). Aerosol particles
38 can negatively impact human health (Partanen et al 2018; Mack et al., 2020), and influence
39 Earth's energy balance. They exert direct effects by scattering and absorbing the incoming solar
40 radiation, altering net radiative fluxes (Charlson et al., 1992; Bond et al., 2013; IPCC, 2021),
41 and indirect effects by acting as cloud condensation nuclei (CCN) and ice nucleating particles
42 (INP), thereby modulating cloud microphysical properties and precipitation processes
43 (Twomey, 1974; Albrecht et al., 1989; Ramanathan et al., 2001; Rosenfeld et al., 2008; Ariya
44 et al., 2009; Burkart et al., 2021).

45 In particular, the Houston region experiences highly complex aerosol processes due to
46 elevated local emissions, diverse aerosol sources, and intricate atmospheric chemistry. One
47 such process is new particle formation (NPF), which is a common aerosol microphysical
48 process that impacts the overall aerosol number concentration (Kulmala et al., 2004; Kerminen
49 et al., 2005; Kuang et al., 2008; IPCC 2013). NPF events typically include a sudden burst of
50 aerosols, i.e., the nucleation of gas molecules and formation of stable clusters of diameters
51 'Dp' > 2 nm, followed by subsequent growth, firstly to a size range with Dp > 50 nm and
52 possibly growing to a size where the particles can act as a CCN (Dp > 100 nm) (Yu and Luo,
53 2009; Kerminen et al., 2012; Gordon et al., 2017). In addition, mesoscale meteorological
54 phenomenon around Houston, such as sea breeze circulations (SBCs), further modulate these
55 aerosol dynamics (e.g., Miller et al., 2003; Wang et al., 2024; Deng et al., 2025; Thompson et
56 al., 2025). These SBCs develop regularly in the warm season along coastal regions (Miller et
57 al., 2003). One key challenge for aerosol process studies common to coastal city environments
58 is in determining the relative importance of aerosol microphysical versus mesoscale
59 meteorological controls such as SBCs, in governing the aerosol number budget and aerosol
60 impacts on that population center.

61 The summertime SBC is a thermally-driven feature tied to differential heating between
62 the land and sea; this results in density gradients that cause the cooler marine air to propagate

Deleted: SBC,

64 inland (Miller et al., 2003; di Bernardino et al., 2021). Daytime SBC formation can facilitate
65 convective cloud and precipitation onset (Comin et al., 2015), influence boundary layer
66 meteorology (Adaricheva et al., 2023), and has been associated with complex impacts on
67 overall air quality (Simpson, 1994; Masselink and Pattiaratchi, 1998; Moorthy et al., 2003;
68 Miller et al., 2003; Augustin, et al., 2020; Park et al., 2020; Parajuli et al., 2022; Wang et al.,
69 2023). These circulations also influence transport of atmospheric gases (Gangoiti et al., 2001;
70 Ahmadov et al., 2007; Hernández-Ceballos et al., 2015) and aerosol particles (Clappier et al.,
71 1999; Borge et al., 2008; Papanastasiou et al., 2010). A sea breeze front (SBF), which is the
72 boundary between that cooler, more moist marine air of the SBC flow and the warmer, drier
73 air over the land, is often a focal point that facilitates the transport and dispersal of aerosols, as
74 well as aiding in the formation of cumulus clouds (Miller et al., 2003). While low-level lapse
75 rates are often more stable on the maritime side of the SBF, the conditional instability
76 (Convective Available Potential Energy-CAPE) is often observed to be greater on the maritime
77 side due to the higher moisture content in that air mass (Hanft and Houston, 2018; Sharma et
78 al., 2024; Boyer et al., 2025). Convergence along these SBFs often results in enhanced upward
79 air motion, allowing aerosols to ascend to higher altitudes ~2 km (Iwai et al., 2011). Stronger
80 wind shear along these SBFs also generates increased turbulence, as owing to Kelvin-
81 Helmholtz instability occurring just behind this front (Linden and Simpson, 1986; Plant and
82 Keith, 2007), while the aforementioned vertical air motions are important for convective cloud
83 initiation (Rao and Fuelberg, 2000; Arrillaga et al., 2020).

84 The common conceptual model for SBCs is one where the marine air mass propagates
85 inland, bringing with it different atmospheric and aerosol characteristics compared to the
86 ambient land air mass conditions. In this study, the influence of these SBCs on regional aerosols
87 is termed as “sea breeze - aerosol interaction” (SAI). Previous studies have shown that SAIs
88 vary depending on complex interactions among emissions sources, boundary layer dynamics,
89 and the strength and/or direction of the SBC (Miller et al., 2003; Boyouk et al., 2011; di
90 Bernardino et al., 2021). For example, SBF passage has been found to trap aerosols at lower
91 elevations within the boundary layer (Miller et al., 2003). In SBC environments, competing
92 processes can yield opposite aerosol responses, as the formation of a shallow thermal boundary
93 layer can confine particles near the surface and raise aerosol concentrations, whereas inland
94 buoyant (convective) lifting within the convective boundary layer, can lift aerosols aloft
95 (Simpson, 1994; Boyouk et al., 2011; di Bernardino et al., 2021). In addition, SBCs may

96 replace the regional air mass with the cleaner marine air mass, leading to a decrease in surface
97 aerosol concentration. This now-modified coastal environment can affect the generation and
98 growth of aerosols, impacting the local aerosol number budget that further influences their
99 direct and indirect effects.

100 Although several studies have investigated the overall change in the aerosol loading
101 during SBC events, less is known about the role of SAI on the aerosol microphysical properties.
102 Moorthy et al. (1993) observed that the passage of the SBF was associated with an increase in
103 the concentration of smaller particles. Furthermore, since SBFs propagate inland, SBCs can
104 have far-reaching impacts on aerosol properties (Iwai et al., 2011; Park and van den Heever,
105 2022). As an example, previous studies conducted in the Southeastern United States indicated
106 that inland propagating SBFs are followed by air masses that often contrasted with regional air,
107 having potential influence on distances 220 km from the Gulf of Mexico (Viner et al., 2021;
108 Bao et al., 2023). In a similar case of these farther-reaching influences, Parajuli et al. (2020)
109 found that the SBC influences the aerosol vertical distribution over the eastern coast of the Red
110 Sea while lifting dust aerosols along the western slope of the Sarawat mountains, with the
111 elevated dust at a height of ~1.5 km over the mountains. Similarly, Talbot et al. (2007) observed
112 that enhanced turbulent activity along the SBF facilitated vertical aerosol transport above the
113 boundary layer top (~1.1 km a.s.l) over a flat coastal area of the North Sea.

114 Finally, high aerosol concentrations in the Houston area are linked to strong surface
115 emissions and meteorological conditions (Wert et al., 2003; Ryerson et al., 2003). This metro
116 region is also home to numerous petrochemical factories that are one of the sources of
117 anthropogenic emissions. Several studies have also shown that meteorological conditions
118 around Houston are highly susceptible to the interaction between large-scale (background)
119 geostrophic flows and mesoscale SBCs (Miller, 2003; Wang et al., 2024; Deng et al., 2025).
120 Pinto et al., (2014) observed that wind direction reversals bring aged, aerosol laden plumes
121 with high O₃ and NO_x levels back to the Houston area. They found that easterly winds,
122 originating from the Houston Ship Channel (HSC), are most strongly associated with elevated
123 levels of photochemically produced species. Similar conditions that promote O₃ and NO_x build-
124 up also drive secondary particle formation, leading to increases in aerosol number
125 concentrations. These particle-phase enhancements in total number concentration result in
126 higher aerosol concentration in the air mass transported from the east. Occasional increases in
127 aerosol concentrations around the greater Houston metropolitan area can also be associated

128 with long-range transported aerosols. At the synoptic scales, the circulation patterns modulate
129 regional meteorology over the Gulf coast. The Bermuda-Azores High helps trans-Atlantic
130 transport of North African dust to the southeast coast (Perry et al., 1997; Bozlaker et al., 2013).
131 Summertime conditions are notably influenced by episodic transboundary aerosol transport
132 (Mao et al., 2020; Das et al., 2023), including dust events from the Sahara Desert (Aldhaif et
133 al., 2020) and biomass burning events in Central America and its neighboring states. The
134 biomass burning includes prescribed agricultural fires in Central America (Wang et al., 2018)
135 and forest fires in surrounding states (Westenbarger and Morris, 2018). Central America
136 biomass burning contributes to half of the biomass burning particulate matter concentrations
137 in Houston (Das et al., 2023). The motivation of this study is to investigate the role of SAIs as
138 observed over a complex urban megacity region, and specifically document SBC influence on
139 aerosol microphysical properties. These efforts expand on previous air quality studies over
140 Houston, including Li et al. (2020) who employed a K-Means clustering algorithm to study the
141 relationship between Houston-region SBCs and the daily ozone variability during the
142 DISCOVER-AQ (Deriving Information on Surface Conditions from Column and Vertically
143 Resolved Observations Relevant to Air Quality) field campaign. While Li et al. (2020) focused
144 on gas-phase chemistry, the same emissions and meteorological processes that drive ozone
145 variability can also influence aerosol loading over the southern Texas region.

146 This study capitalizes on the TRacking Aerosol Convection Interactions ExpeRiment
147 (TRACER) field campaign conducted by the US Department of Energy (DOE) Atmospheric
148 Radiation Measurement (ARM) user facility (Mather and Voyles, 2013), which took place
149 from October 1, 2021, to September 30, 2022 (Jensen et al., 2022; 2025). The main TRACER
150 field site was placed at an urban coastal location in Houston. As in TRACER's overarching
151 motivations, the Houston region is frequented by isolated convective clouds that interact with
152 ambient aerosol conditions from the urban and industrial sources, potentially serving as a
153 natural contrast to clouds that form in surrounding areas that exhibit significantly lower
154 background aerosol concentrations (Banta et al., 2011; Parrish et al., 2009; Wang et al., 2024;
155 Thompson et al., 2025). Additional observations were made at a rural coastal site (supplemental
156 site) in southern Texas during an intensive observation period (IOP) from June 1 to September
157 30, 2022. Using these TRACER-IOP measurements, our study explores how these SBCs
158 influence the aerosol environment at multiple ground sites. In addition, the Weather Research
159 and Forecasting model coupled with Chemistry (WRF-Chem) is used to investigate the

160 regional impacts of SAI over Southern Texas. A detailed description of the TRACER sites,
161 instruments, measurements, and methodology, followed by the WRF-Chem model
162 configuration details, are presented in Section 2. Section 3 presents campaign observational
163 and simulated results. Our efforts will characterize the composite meteorological (Section 3.1)
164 and aerosol (Section 3.2) observations during the IOP at the TRACER main and supplemental
165 sites. This is followed by a composite analysis of the observed effects of the sea breeze on
166 aerosol properties at the two ARM sites (Section 3.3), as well as a detailed case study
167 examination of SAI influence for these locations (Section 3.4). The regional influence of SAI
168 is further explored using model simulations, as demonstrated for the horizontal (Section 3.5)
169 and vertical propagation of SAIs (Section 3.6), and SAI impact on cloud condensation nuclei
170 over the southern Texas region (Section 3.7). The study concludes with our key findings
171 summarized in Section 4.

172

173 **2 Data and methods**

174 2.1 Site description

175 The DOE ARM TRACER field campaign was centered on the deployment of the first ARM
176 Mobile Facility (Miller et al., 2016, herein AMF1) at the main instrument site (M1) (Fig. 1).
177 The M1 is an urban coastal site located at the La Porte, Texas (TX) airport, to the southeast of
178 Houston, TX. Given the high propensity for isolated convective cloud events during
179 summertime months (Jensen et al., 2022; 2025), the TRACER IOP was conducted from June
180 1 to September 30, 2022, with a goal towards sampling a range of aerosol-cloud interactions
181 during these convective events. Additional ARM and guest instruments were deployed to a
182 supplemental site (S3) during the IOP as documented in Jensen et al. (2022). The S3
183 supplemental site is a rural coastal site in Guy, TX, located ~70 km west from M1, upstream
184 and periphery to the highly populated and commercial sectors of the Houston-Galveston-
185 Brazoria region.

186 The southern Texas region is characterized by flat terrain with elevations < 50 m a.s.l and
187 a diversity of land cover/use, including urban, rural, grassland, and forested coastal
188 environments (see Fig. 2a). Although both the M1 and S3 sites are a similar distance from the
189 Gulf of Mexico, the M1 site is located near the western shore of Galveston Bay. This urban

190 M1 site may experience different sea-breeze timing because of its location, the added influence
191 of the Galveston Bay breeze, and urban heating that alters local circulations. The M1 site is
192 expected to be strongly influenced by anthropogenic activities due to its proximity to the
193 Houston urban core, large-scale industrial complexes and the HSC. The HSC is lined with
194 dense clusters of industrial facilities, including major petrochemical complexes (Yoon et al.,
195 2021), which can contribute to aerosol populations beyond those typically associated with an
196 urban environment. Similarly, the Texas A&M University (TAMU) TRACER measurements
197 also showed that short-lived ship emissions contributed to high aerosol concentrations (up to
198 $34,000 \text{ cm}^{-3}$) (Rapp et al., 2024; Thompson et al., 2025). The S3 site, while relatively less
199 impacted by the emissions from the Greater Houston area, is not representative of a pristine
200 rural location in terms of aerosol loading. Under typical south-southeasterly wind, this S3 site
201 is located downstream of heavy industry along the southeast Texas coastline (Freeport, TX and
202 Lake Jackson, TX) and can be influenced by upstream anthropogenic sources (Fig. 2b).

203

204 2.2 Measurements of aerosols and meteorological properties

205 This study focuses on the enhanced aerosol and complementary observations available
206 during the TRACER summertime IOP period. The key aerosol datasets available during this
207 IOP include: (1) the aerosol number size distribution and total number concentration, (2) bulk
208 aerosol chemical composition, and (3) state meteorological properties (e.g., surface
209 temperature, humidity). Campaign availability of in-situ observations at two contrasting sites
210 provided an excellent opportunity to understand the regional aspects of SAI.

211 The aerosol number size distribution with diameter ranging from 10 to 500 nm was
212 measured at M1 and S3 sites using Scanning Mobility Particle Sizer (SMPS) (Singh and Kuang,
213 2024). The aerosol number size distributions ($dN/d\log D_p$) (aerosol number concentrations in
214 different diameter bins) at different diameters (D_p) were added to calculate the total integrated
215 aerosol number concentrations. Bulk aerosol chemical compositions consisting of total
216 organics, sulfate, nitrate, ammonium, and chloride were measured at M1 and S3 sites using
217 Aerosol Chemical Speciation Monitor (ACSM) (Watson, 2017). Surface meteorological
218 variables: temperature, water vapor mixing ratio (w), wind direction and wind speed at M1 and
219 S3 sites were taken from the meteorological instruments collocated with the aerosol
220 instruments. All of these instruments are part of the ARM Aerosol Observing Systems (AOS),

221 which is the platform for in situ aerosol measurements at Earth's surface (Uin et al., 2019).
222 Missing data were excluded from this analysis. If more than 20% of the data were missing
223 during the 5 hours before and after the passing of the SBF, the dataset was not used to study
224 SAI processes. SMPS and ACSM sample data at 5-minute and ~30-minute intervals,
225 respectively. State meteorological variables were observed at one second intervals. All
226 datasets, except for the ACSM, were averaged over a 5-minute interval, centered on the time
227 of the SMPS sample.

228 To supplement the ARM observations, we use particulate matter of 2.5 micrometers or less
229 in diameter ($PM_{2.5}$) mass concentrations from the Texas Commission on Environmental
230 Quality (TCEQ) database (Shrestha et al., 2023; sfcmetradaq-tceq ARM PI product). Although
231 TCEQ operates a broad network of air quality monitoring stations throughout Texas, the
232 Seabrook Friendship Park site (C45, $-95.02^{\circ}E$, $29.58^{\circ}N$) was selected because it is the nearest
233 monitor to the M1 site (~6 km away) and provided continuous hourly $PM_{2.5}$ data during the
234 study period. $PM_{2.5}$ was chosen as a representative aerosol to directly compare with the model
235 simulations. For reference, this TCEQ C45 site location was added to the map displaying the
236 TRACER sites (Fig. 1).

237 This study draws heavily from SBC synoptic-scale regime identification performed by
238 Wang et al. (2024) to further inform on controls affecting SBC evolution and cloud formation
239 at the two sites. Every SBC day identified by Wang et al. (2024) during the IOP period is
240 considered to explore SAI during TRACER. A total of 46 SBC events at the M1 site, and 30
241 SB events at the S3 site were identified by Wang et al. (2024) during TRACER's IOP (Table
242 1). They explored Gulf breeze and bay breeze circulation characteristics using a suite of
243 datasets, including ground-based measurements, satellite observations, and reanalysis datasets,
244 using machine learning techniques, and Lagrangian cell tracking methods. Most IOP SBC
245 events were classified as occurring during large-scale anticyclonic conditions, with the
246 predominant occurrence of SBCs observed during southeasterly background surface wind
247 directions. The SBF timing at both ARM sites was determined using surface wind and w mixing
248 ratio time series.

249 Overall, Wang et al., (2024) found that the SBF typically arrived at the M1 site at 20:30
250 UTC (i.e., 15:30 LT), and at the S3 site at 20:50 UTC (i.e., 15:50 LT). The M1 site, situated
251 along the western shore of the Galveston Bay, was also influenced by bay breeze circulations,
252 frequently resulting in an earlier shift in the local meteorological state compared to that of the

253 S3 site (only influenced by the Gulf SBC). The M1 site was shown to experience an additional
254 bay breeze contribution during 22 out of 43 SBC events. Wang et al. (2024) also reported that
255 M1 experienced higher intensity changes in the meteorological conditions associated with these
256 SBFs as compared to S3, particularly when the background wind directions are southwesterly
257 or westerly. At both the sites, these SBF passages were associated with a significant increase
258 in w and wind speed, along with a decrease in surface temperature. The arrival of the fronts
259 also typically increased the vertical wind speed within the boundary layer, with a mean speed
260 of up to 2 m s^{-1} within the lowest 1 km. The enhanced updrafts associated with SBF low level
261 convergence also was shown to promote short lived-isolated convective clouds and likely
262 associated with vertical mixing of aerosols by diluting near-surface concentrations and
263 redistributing aerosols aloft.

264

265 2.3 Model simulation setup

266 The WRF-Chem model (Grell et al., 2005; Skamarock et al., 2008) was used to simulate
267 the multiscale interactions between aerosols and meteorology over the coastal region of
268 southeast Texas. Fig. 2 shows the model domain centered on the M1 site and extended from
269 26 to 33 °N (~770 km) in latitude and from -98.5 to -91.5 °E (~770 km) in longitude. The model
270 simulations were performed for the period from 1 July to 30 August 2022, using a 5x5 km
271 horizontal grid spacing with 45 vertical layers. A model spin-up time of 3 days was used, and
272 the restart files were used for the remainder of the simulations. Initial and boundary conditions
273 for meteorology were provided by the North American Mesoscale (NAM) model every 6 hours.
274 The model configuration was successfully set-up and is considered sufficient to resolve the key
275 meteorological processes relevant to the aerosol chemistry examined in this study. To validate
276 this assumption, simulated meteorological fields and aerosol variabilities are compared against
277 observations. Similar model setups have been successfully applied in previous WRF-Chem
278 studies over the continental US (e.g., Berg et al., 2015; Wang et al., 2021; Subba et al., 2023;
279 Shrivastava et al., 2024), which demonstrate their suitability for representing aerosol-cloud
280 interactions. The details of the configurations are shown in Table 2.

281 The model simulations were performed with (with aerosol-WA condition) and without (no
282 aerosol-NA condition) full aerosol-gas chemistry, and land-atmosphere interactions enabled.
283 Boundary conditions for gas-phase species and aerosols were provided by the Whole

284 Atmosphere Community Climate Model (WACCM) (Gettelman et al., 2019). The WACCM
285 output datasets, available on a horizontal grid resolution of $1^\circ \times 1^\circ$ were spatially interpolated
286 to our model domain every 6 hours. Biogenic emissions were generated online by WRF-Chem
287 model based on meteorology and land use data, using the Model of Emissions of Gases and
288 Aerosols from Nature version 2.1 (MEGAN2.1) by Guenther et al. (2012). The U.S.
289 Environmental Protection Agency National Emission Inventories (NEI, Ma and Tong, 2022)
290 was used to provide anthropogenic emissions of trace gases and aerosols from diverse sources,
291 including point, area, on-road mobile, non-road mobile, and other sectors. These emissions are
292 incorporated to WRF-Chem at hourly intervals. The area surrounding the M1 site is
293 characterized by urban infrastructure and cropland, whereas the S3 site is largely a mix of
294 cropland, natural mosaic, and barren or sparsely vegetated land type. Both sites have cropland
295 and grassland to the west and north, as well as evergreen, deciduous, and mixed forests from
296 the north to east directions. The selected domain included both anthropogenic and biogenic
297 aerosol sources, as indicated by NEI and MEGAN datasets (Fig. 2b). The M1 site is anticipated
298 to be more influenced by anthropogenic sources due to its proximity to the Houston urban core,
299 local industry and the HSC. The S3 site is expected to be more influenced by biogenic sources.

300 The role for these simulations is to provide a physically-reasonable spatial approximation
301 for the meteorological and aerosol environments across the southern Texas region that are not
302 captured by the point measurements during TRACER. Comparing the meteorological variables
303 between the two sites helps identify the underlying factors that may influence the aerosol
304 transport and transformation processes. The simulated meteorological time series show
305 adequate agreement for the purposes of this study at both sites (Fig. S1). We assessed model
306 performance using metrics: mean bias (MBE), root mean square error (RMSE), and correlation
307 coefficient (R) for the quantities of temperature, wind speed, and wind direction. In addition,
308 we also considered Modern-Era Retrospective analysis for Research and Applications
309 (MERRA-2) reanalysis products to further evaluate the model performance (Geralo et al.,
310 2017). Our model reproduces the measured temperature diurnal cycle at both sites with high
311 correlation (r up to 0.87) and low MBE ($< \pm 1$ °C). Wind speed and wind directions show
312 weaker correlation (r up to 0.65) and MBE of 0.76 m s^{-1} and 12.5° , respectively. Individual
313 SBF events are further analysed to compare the measured and modeled variables in later
314 sections.

315 We find a reasonable behavior in the heterogeneous spatial distribution of PM_{2.5}, with
316 higher values in the urban areas around the M1 site and lower values in the rural areas around
317 the S3 site (Fig. 3b). The simulated hourly PM_{2.5} has been compared with the TCEQ measured
318 values (Fig. 3a). The model reasonably captures the timings and magnitude of high and low
319 aerosol concentrations. The model (mean ~ 10.8 µg m⁻³, median ~8.5 µg m⁻³) overestimates the
320 observations (mean ~8.2 µg m⁻³, median ~7.0 µg m⁻³), with a correlation of $r \sim 0.6$,
321 corresponding to differences of ~30% in the mean and ~ 23% in the median. These model-
322 measurement discrepancies are consistent with previously reported WRF-Chem biases. For
323 example, Soni et al. (2022) reported that during dust storm events over the Indian sub-
324 continent, WRF-Chem captured spatial aerosol patterns but underestimated concentrations in
325 regions of high aerosol loading. Similarly, Tuccella et al. (2012) reported that WRF-Chem
326 underestimated peak aerosol concentrations by 7.3%. More recently, Georgiou et al. (2022)
327 reported underestimation of background PM_{2.5} by 16% and of industrial by ~20%.

328

329 3 Results and discussion

330 3.1 Composite IOP Meteorological Observations

331 Comparisons between the background summertime meteorology around the TRACER
332 sites help to identify the underlying factors that may influence the aerosol transport and
333 transformation processes. Fig. 4. shows composite averaged diurnal variations of
334 meteorological properties during the IOP period. When comparing meteorological variables
335 between M1 and S3 sites, paired t-test results calculated a very low p-value (<0.0001) and a
336 large negative or positive t-statistic, indicating a statistically significant difference. M1 exhibits
337 higher temperatures during the cooler parts of the day (early morning) and slightly lower
338 temperatures during the warmest parts of the day (early afternoon). *w is generally higher at M1*
339 *than at S3 for most hours of the day (Fig. 4b)*. At both sites the value stays near 17-18 g kg⁻¹
340 for most of the day, with a common moistening pulse around 13:00-15:00 UTC that coincides
341 with increased wind speed. *At this time (13-15 UTC)*, the wind directions are similar at both
342 sites. Except in the morning, winds at M1 are typically 1-2 m s⁻¹ stronger than at S3. The
343 M1 site shows an increase in *w* near 20:00 UTC, likely tied to the SBC. S3 exhibits a larger
344 shift in the wind directions compared to that of M1. The two sites have similar directions during

Deleted: *w* at M1 is lower during the warmer periods and higher during the cooler periods of the day

Deleted: At similar hours

348 the late night (00:00- 05:00 UTC) and early morning (13:00-15:00 UTC) hours. During the
349 dominant afternoon SBC period (around 20:00 UTC), winds are predominantly from the
350 southeast at M1 and from the southwest at S3.

351 Although these sites are geographically close, their different proximities to water bodies
352 and varying land cover types may account for the observed meteorological variations, such as
353 differences in temperature modulation, humidity, and breeze development. M1 lies adjacent to
354 both Galveston Bay and Gulf of Mexico, thus nearby water moderates temperature and
355 promotes higher humidity, favoring sea- or bay- breeze circulations. In contrast, although S3
356 is at a similar distance from the Gulf as M1, it is more inland, separated from the shoreline by
357 an intervening expanse of land, so it experiences stronger daytime heating and a weaker, more
358 modified marine influence than M1. It has a land surface covered predominantly with
359 vegetation and soil that cools faster at night than urban landscapes. However, urban landscapes
360 retain heat, remaining warmer into the nighttime and potentially moderating temperatures
361 during the subsequent daytime (Maria et al., 2013). These behaviors are consistent with the
362 prior studies showing the coastal sites experienced moderate temperature and enhanced
363 humidity (Hu, 2021; Subramanian et al., 2023), and that land-use influenced local temperature
364 and boundary layer dynamics via evapotranspiration and surface heating (Fang et al., 2025).

365

366 3.2 Composite IOP Aerosol Observations

367 The southern Texas region is influenced by locally-generated (e.g., vehicular, industrial,
368 construction and road dust, and sea spray) and long range transported aerosols (e.g., biomass
369 burning, mineral dust, and sea spray) from anthropogenic and natural sources (Brown et al.,
370 2002; Barrett and Sheesley, 2014; Karnae and John, 2019; Song et al., 2021; Das et al., 2023;
371 Shrestha et al., 2023). In Fig. 5a, aerosol number concentration peaks around 17:00 UTC at M1
372 and around 20:00 UTC at S3. Both sites exhibit a tri-modal aerosol size distribution (Fig. 5b).
373 Throughout the day, the aerosol concentrations are consistently higher at the M1 site when
374 compared to those observed at the S3 site. At the M1 site, we observe a distinct nucleation
375 mode that appears at diameter <20 nm, and two additional modes at larger diameters ~ 80 nm
376 and ~ 150 nm. This nucleation mode is less prominent at the S3 site, which more commonly
377 exhibits similar modes at diameters ~ 80 nm and ~ 150 nm.

378 The ACSM observations suggest a similar percentage contribution from various species,
379 with organics having the highest concentration (59.2% at M1 and 53.0% at S3), followed by
380 sulfate (23.3% at M1 and 30.6% at S3), ammonium (11.4% at M1 and 10.8% at S3), nitrate
381 (5.2% at M1 and 5.0% at S3) and chloride (less than 0.9% at M1, and less than 0.6% at S3).
382 Higher percentages of organics and sulfate were also measured at other urban (Minguillón et
383 al., 2015; Huang et al., 2010; Qi et al., 2020) and rural locations (Crippa et al., 2014; Atabakhsh
384 et al., 2023).

385 The NPF events are identified by analyzing the aerosol size distribution measured by the
386 SMPS (Kuang et al., 2008; Dal Maso et al., 2002; Mikkonen et al., 2011). This is accomplished
387 by designating characteristic features for NPF found in the size distribution behaviors in time,
388 including the appearance of the nucleation mode at a diameter (D_p) < 25 nm, followed by
389 distinct growth pattern (where the particles increase in size over several hours) forming the
390 characteristic “banana-shaped” pattern in the aerosol number size distribution. NPF events
391 were common at both the M1 and S3 sites. During summertime, NPF events were identified at
392 both the M1 and S3 sites, finding 23 and 17 events, respectively. In approximately 35% of
393 cases, NPF events were observed simultaneously at the sites, implying a regional-scale
394 behavior. These regional NPF nucleation modes appear at D_p < 25 nm and grow consistently
395 across a broader region, covering a minimum radius of tens of kilometers. Recent study by
396 Kasparoglu et al. (2025) also observed NPF events attributed to nucleation aloft with daytime
397 turbulent mixing transporting the growing mode downward, consistent with unsteady ultrafine
398 aerosol number concentrations, gradual increases, and absence of <20 nm growth near the
399 surface. The growing-mode hygroscopicity spanned 0.05-0.34, varied by wind sector,
400 implicating changes in precursor chemistry across air masses. Thus, the differing
401 characteristics of simultaneous NPF events are plausibly driven by mesoscale to large-scale
402 meteorological controls on these processes (such as SBCs), the prevailing condensation sink
403 from background aerosol, and/or the availability of precursors in each air mass.

Deleted: However, these simultaneously-occurring NPF events displayed different characteristics in terms of their duration and growth, hinting at the possible influence of mesoscale to larger-scale meteorological controls on these processes (such as SBCs), the background aerosol concentration and/or the availability of necessary precursors.

404

405 3.3 Observed Sea Breeze aerosol interaction at the surface

406 Coastal regions have a mixture of urban, terrestrial, and marine aerosol regimes. The
407 inland-penetrating SBF can have a complex influence on the aerosol populations over Houston
408 and its surroundings depending on several coexisting factors including: (i) the pre-existing

415 aerosol regime over the location, (ii) the aerosol regime of the air mass preceded by the SBF,
416 (iii) the local to synoptic thermodynamic conditions resulting from convective boundary layer
417 features such as horizontal convective rolls, and (iv) the characteristics of the SBF itself,
418 including the lifting and mixing of the onshore flow with the ambient air, and wind anomalies
419 near the surface. Three scenarios for the influence of an inland-penetrating SBF on aerosols
420 within the region of influence are considered.

421 First, we consider a potential “reduction influence” that may occur when an air mass with
422 higher aerosol concentration over a location is replaced by an air mass with lower aerosol
423 concentration. In contrast, an “enhancement influence” may occur when an air mass with lower
424 aerosol concentration over a location is replaced by an air mass with higher aerosol
425 concentration. Otherwise, a “neutral influence” implies minimal change associated with the
426 SBF, defined as a change in the aerosol concentration is less than 5% in the pre-existing aerosol
427 regime. This scenario indicates that the air mass following the SBF is similar to the existing
428 conditions.

429 For example, these enhancement influence scenarios may be anticipated when long-range
430 transported aerosols are present in the air mass downwind of the SBF, or when the SBF first
431 advects over areas (marine or continental) with high local emissions. Similarly, neutral
432 influence scenarios are anticipated when the entire region has relatively homogeneous (i.e.,
433 similar aerosol concentrations also belonging to the same aerosol regime) distribution of
434 aerosols. Nevertheless, aerosol exchanges are complex, and TRACER also provided several
435 examples of marine aerosols carried by the SBF that were associated with negligible influences
436 on the ambient marine aerosol mode. Finally, TRACER site measurements may not always be
437 representative of a broader air mass or regional conditions (e.g., intermittent local source
438 interactions with smaller-scale SBC features). WRF-Chem modeling may help to bridge these
439 spatial representativeness gaps and provide reference for the regional context of the potential
440 impact of the SBC on aerosol distributions.

441 To investigate the influence of SAI, one approach employed in this study is to normalize
442 the surface aerosol concentration at time T by the value measured immediately before the
443 passing of the SBF ($T_{\text{SBF}}=0$ hour). The timing of the SBF for each event is explicitly
444 considered, using the passage times provided in Table A1 on Wang et al. (2024). The SBF
445 passage at a site is defined as $T_{\text{SBF}}=0$. This approach allowed evaluation of aerosol number
446 concentrations before and after the SBF passage while retaining the diurnal cycle context. Here,

447 “just before” refers to the five minutes prior to the SBF passage, as previously identified by
448 Wang et al. (2024). Figs. S2 and S3 show the temporal variation of this normalized aerosol
449 number concentration for all the SB events. At both the M1 and S3 sites, before-SBF aerosol
450 concentrations can vary by up to a factor of two.

451 Example days with an “enhancement influence” in the aerosol concentration after T_{SBF} are
452 shown in Fig. 6, highlighting the 18 July event at the M1 site, and a 10 August event at the S3
453 site. In contrast, the 17 June (M1 site) and 10 July (S3 site) events in the same figure help
454 illustrate a “reduction influence” in aerosol concentration after T_{SBF} . While these example
455 events are instructive, there is not a clear trend for TRACER events given the high level of
456 variability in the duration or influence of SAIs. For example, the sharp increase we observe in
457 aerosol concentration on the 10 August “enhancement” event quickly dissipates within an hour
458 after T_{SBF} at the S3 site. In contrast, the increase in the number concentration we observed on
459 18 July persisted for over an hour after T_{SBF} . Considering all the SBF passages we collected
460 (Figs. S2 and S3), we suggest $\Delta T = T_{\text{SBF}} \pm 1$ hour often best represents the “before” ($\Delta T = T_{\text{SBF}}$
461 - 1 hour) and “after”- SBF ($\Delta T = T_{\text{SBF}} + 1$ hour) times over a location. The enhancement or
462 reduction effects are most pronounced during the first hour following the passing of the SBF.
463 Beyond this period, the observed changes may be influenced by additional factors, such as the
464 secondary effects resulting from meteorological transitions induced by the SBF. Additionally,
465 the intensity of the SBF’s impact may begin to weaken or become less pronounced after the
466 first hour. With that assumption, a percentage change of the aerosol number concentration
467 [(after-before)/before x 100%] can be further calculated. ‘Neutral influence’ days with the
468 change in aerosol concentration <10% are not considered in this analysis.

469 Table 1 summarizes the total number of SBC events, along with number and percentage of
470 days showing enhancement, reduction, or neutral influence on the aerosol number
471 concentration at the M1 and S3 sites. Neutral days were excluded from the overall averages to
472 focus solely on the cases with a clear aerosol response. Out of 46 SBC events at the M1 site,
473 29 events (~63%) showed an enhancement or reduction influence on total aerosol number
474 concentration, while the remaining 17 events (~37%) were classified as having a neutral
475 influence. In contrast to M1, at the S3 site, out of 30 SBC events, only 12 events (~40%)
476 exhibited a detectable change in aerosol number concentration, with the remaining 18 days
477 (~60%) considered neutral. At the M1 site, reduction events (16 events) slightly outnumbered
478 enhancement events (13 events). In contrast, at S3, enhancements (8 events) were twice as

479 common as reductions (4 events). This opposite pattern underscores the site-dependent nature
480 of the sea-breeze influence.

481 During enhancement days, the M1 site shows an average increase in aerosol number
482 concentration of ~ 55%, rising from $3.8 \times 10^3 \text{ cm}^{-3}$ during ΔT^- to $5.9 \times 10^3 \text{ cm}^{-3}$ during ΔT^+ . In
483 contrast, during the reduction days, the concentration decreases by ~ 42%, dropping from $13.2 \times$
484 10^3 cm^{-3} during ΔT^- to $7.6 \times 10^3 \text{ cm}^{-3}$ during ΔT^+ . At the S3 site, the average changes are ~64%
485 (from $2.4 \times 10^3 \text{ cm}^{-3}$ during ΔT^- to $3.9 \times 10^3 \text{ cm}^{-3}$ during ΔT^+) enhancement and ~45% (from
486 $4.9 \times 10^3 \text{ cm}^{-3}$ during ΔT^- to $2.7 \times 10^3 \text{ cm}^{-3}$ during ΔT^+) reduction. When averaged across all
487 events, the aerosol number concentration at M1 shows a net decrease of ~23%, from 8.9×10^3
488 cm^{-3} during ΔT^- to $6.8 \times 10^3 \text{ cm}^{-3}$ during ΔT^+ , while S3 exhibits a net increase of ~9%, from
489 $3.2 \times 10^3 \text{ cm}^{-3}$ during ΔT^- to $3.5 \times 10^3 \text{ cm}^{-3}$. These contrasting trends underscore the regional
490 variability in aerosol responses associated with SAI events.

491 As previously mentioned, the geographical positioning of M1 and S3 sites could be one of
492 the reasons for such variabilities. M1 is more influenced by the bay breeze coming from
493 Galveston Bay and S3 is more likely influenced by Gulf breeze from Gulf of Mexico. Even if
494 the SBF air mass initially contains lower aerosol concentrations, a longer inland transit to S3
495 can (a) increase mixing with the preexisting continental boundary layer and (b) increase
496 acquisition of continental emissions along the over-land fetch, either of which can raise
497 concentrations by the time the SBF reaches S3, and vice versa. The M1 site is influenced by
498 the air masses and SBCs from both sources, whereas the S3 site is affected predominantly by
499 those originating from the Gulf of Mexico. As discussed in detail by previous studies (Sharma
500 et al., 2024; Wang et al., 2024), the SBFs originating from Galveston Bay and the Gulf of
501 Mexico are often distinct at onset but tend to merge later in the afternoon or evening. Due to
502 the M1 site's proximity to Galveston Bay, it is more directly influenced by maritime air masses
503 that are heavily modified by Galveston Bay as the SBF originating from the Gulf of Mexico
504 traverses the Bay. On the other hand, the Gulf-originating SBF must cross land before reaching
505 S3. The difference in SBF pathways can lead to notable meteorological and aerosol contrasts
506 between the two sites. In addition, as observed by Thompson et al. (2025), the maritime air
507 masses near Galveston can deviate significantly from typical clean maritime conditions. As a
508 result, bay breeze passages may not always lead to cleaner air but can, in fact, be more polluted.
509 The consequences of this increased aerosol concentration in the modified maritime air mass
510 are reflected in the enhancement aerosol response observed at the M1 site.

Deleted: Even if the air mass associated with the SBF contains lower aerosol concentration, the longer distance the SBF travels to reach the S3 site allows the marine air mass to mix with the continental air mass, potentially resulting in higher aerosol concentrations

516 SAs can also interfere with NPF events. On SB days, a total of 7 NPF events were observed
517 at the M1 site and 4 at the S3 site, with 3 occurring simultaneously at both sites. Among these,
518 45% (5 out of 11) events showed distinct changes in NPF characteristics during the SBF
519 passage. For example, on 16 July an NPF event was observed at M1 prior to the SBF (Fig. S4).
520 With the arrival of the SBF, particle growth abruptly ceased, and the elevated particle
521 concentration ($\sim 14 \text{ e}^3 \text{ particles cm}^{-3}$) rapidly decreased to $\sim 5 \text{ e}^3 \text{ particles cm}^{-3}$ (Fig. S4). The
522 normalized aerosol size distribution further shows that the NPF activity evident in the hours
523 before the SBF period ($\Delta T = T_{\text{SBF}} - 1 \text{ hour}$) disappeared in the hour following the SBF
524 ($\Delta T = T_{\text{SBF}} + 1 \text{ hour}$). The low aerosol concentration air mass trailing the SBF passage thus led
525 to a sharp reduction in the aerosol number concentrations in the after-SBF period.

526 The open-air polar plots summarize the relationship between aerosol number concentration,
527 wind speed and wind direction within $\Delta T = T_{\text{SBF}} \pm 1 \text{ hour}$ during enhancement and reduction
528 events (Fig. 7). At M1, enhancement events reveal elevated aerosol concentrations when the
529 prevailing winds emanate from the east and southeast, where the air mass is influenced by
530 industry and shipping along Galveston Bay. During the reduction influence the pre-SBF aerosol
531 loading is higher compared to that of the reduction events. These high concentrations are
532 associated with the influence from the Houston urban core in the northwest and the other
533 influences from the east as mentioned above. These are also apparent in the monthly plots
534 shown in Fig. S5. After-SBF winds, particularly from the southeast and south, are associated
535 with markedly lower aerosol loads, indicative of cleaner marine air intrusion.

536 Meanwhile at S3, enhancement scenarios also manifest somewhat higher concentrations
537 when winds shift southeastward, though to a lesser extent, reflecting rural aerosol dynamics.
538 In reduction scenarios at S3, aerosol levels decrease most notably under southerly and
539 southwest flow, reinforcing the interpretation that sea breeze incursions generally replace
540 continental aerosol-laden air with cleaner marine air at both sites, albeit with stronger source
541 influence at M1. This wind-direction-dependent concentration pattern aligns with previous
542 findings: northwesterly to easterly winds bring continental aerosols, while southerly to
543 southwesterly flows usher in marine-influenced clean air that modulates aerosol number
544 concentrations (Levy et al., 2013; Pinto et al., 2014). [Recent study by Kasparoglu et al. \(2025\)](#)
545 [observed that the cloud droplet number concentrations differed by a factor of \$\sim 2\$ -3 between](#)
546 [northeasterly and southerly flows, highlighting strong wind-direction controls on cloud](#)

547 [microphysics around southern Texas](#). However, as shown in Figs. S2 and S3, each SB event is
548 unique in terms of the change in the aerosol concentrations.

549

550 3.4. Examples of sea breeze aerosol interaction at the TRACER sites

551 In Fig. 8, we provide an example of an aerosol reduction influence of SAI. Since M1 and
552 S3 both experienced the passage of a SBF on 10 July, this day serves as a good example to
553 investigate how SAIs evolve when simultaneously viewed at multiple sites. The SBF reached
554 the M1 site in the afternoon at around 21:30 UTC, and the S3 site at around 23:45 UTC. In Fig.
555 S6, we supplement these discussions with displays for the temporal variation of measured and
556 model-simulated meteorological properties for this event. Both sites suggest the typical
557 temperature decreases and surface wind speed increase associated with the SBF reaching the
558 site. The wind direction changes from east to south at the M1 site and from southwest to south
559 at the S3 site.

560 The changes in aerosol size distribution, reduction in the bulk chemical composition, and
561 simulated $PM_{2.5}$ all suggest that the air mass following SBF passage contains lower aerosol
562 concentration (Fig. 8.). This likely indicates that during the after-SBF period, the air mass is
563 arriving from directions less influenced by the aerosol sources. The SBF acts as a leading edge
564 of this cleaner marine air mass. The aerosol number concentration decreases by $\sim 5\%$ (5.2 e^2
565 cm^{-3}) at the M1 site. At the M1 site, there was no significant change in the mean D_p ($\sim 100 \text{ nm}$)
566 during the first 45 min after T_{SBF} , which is followed by a sharp decrease in the mean D_p (~ 25
567 nm). This change in the aerosol number concentration is synchronous with the changes in wind
568 directions. During the after-SBF period, the winds shift predominantly from the southeast and
569 south, bringing in a more marine-influenced air mass.

570 Immediately after the passing of the SBF at the S3 site, the SAI also indicates a
571 reduction of the aerosol number concentration by $\sim 62\%$ ($3.3 \text{ e}^3 \text{ cm}^{-3}$) (Fig. 8b). However, the
572 background aerosol mode persists at diameters ~ 60 and 150 nm (aerosol size distribution plot
573 in Fig. 8b). Note, we did not observe a profound change in the wind directions after the passing
574 of the SBF at the S3 site. However, we suggest that the higher wind speed associated with the
575 SBF dilutes the existing air mass with marine air with lower aerosol concentration. Higher
576 wind speeds enhance near-surface shear, mechanically generate turbulence, deepen the
577 boundary layer, and strengthen vertical transport, thereby accelerating dispersion and diluting

578 aerosol and water-vapor concentrations (Kgabi and Mokgwetisi, 2009; Dueker et al., 2017; Liu
579 et al., 2025). Conversely, low winds with a shallow boundary layer and weak turbulence
580 promote accumulation and often worsen air quality due to limited dilution (Seinfeld and Pandis,
581 2006). The modified near-surface air mass at S3 persists overnight until convective mixing
582 begins the following day. Under stable stratification, buoyant turbulence is suppressed, and
583 shear-driven mixing becomes the primary dilution mechanism; although weaker than
584 convective mixing, it can still substantially mitigate concentration build-up (Rodier et al.,
585 2017).

586 The aerosol bulk chemical mass concentration at the M1 site shows a steady buildup
587 through the day, peaking just before the passing of the SBF. Organics were the dominant
588 species throughout, with sulfate and nitrate also contributing. After the passage of the SBF,
589 concentrations dropped rapidly by about 1 to 3 $\mu\text{g m}^{-3}$, with the drop being more apparent in
590 sulfate and organics. Within a few hours, concentrations returned to the background levels.
591 These concentrations remained higher than those at the rural S3 site. However, the more
592 pronounced changes in aerosol properties were observed at the S3 site. The concentrations of
593 all species, including organic, decreased by 2 to 3 $\mu\text{g m}^{-3}$. This is consistent with the earlier
594 discussion that the maritime air mass near Galveston Bay exhibits higher aerosol
595 concentrations compared to the more pristine maritime air mass originating directly from the
596 Gulf of Mexico.

597 In Figs. S7 and S8, we provide additional examples from TRACER SAI events. The first
598 example is from the 17 July event where we observed an increased influence in the aerosol
599 concentration that followed SBF passage. In Fig. S7, we present an example of an aerosol
600 enhancement case associated with an SAI event on 17 July. The SBF reached the M1 site in
601 the early afternoon (~18:12 UTC), and at around 21:42 UTC at the S3 site. The aerosol size
602 distribution displayed an enhancement of particles in the diameter range of 15-100 nm. Total
603 organics, sulfate, and simulated $\text{PM}_{2.5}$ also increased, suggesting that the post-SBF air mass
604 contained higher aerosol concentrations, likely due to transport from more polluted source
605 regions. Similar to the 10 July case, the SBF acted as the leading edge, but here it marked a
606 more polluted marine-influenced air mass.

607 At M1, the aerosol number concentration also doubled ($\sim 2.2 \times 10^3 \text{ cm}^{-3}$), accompanied by a
608 significant shift in mean particle diameter (within 15-100 nm) during the first hour after SBF
609 passage, with weaker changes thereafter. These responses were synchronous with shifts in wind

Deleted: ammonium

611 direction from southwest to east. The easterly winds, influenced by emissions from the HSC,
612 contributed to the observed increase. In contrast, at S3 the SAI did not produce distinct changes
613 in aerosol size distribution or mass concentrations, and except for the increase in the wind
614 speed, no substantial wind direction change occurred after SBF passage. The modified near-
615 surface air mass at both sites persisted for only ~2 hours, after which background conditions
616 returned. Notably, background aerosol modes at ~60 nm and ~150 nm persisted throughout
617 (Fig. S7).

618 Fig. S8 shows an example of a neutral SAI influence on 16 August. The SBF reached M1
619 at ~17:05 UTC and S3 at ~20:10 UTC. At M1, winds shifted from east to south, while no
620 distinct directional change was observed at S3. Unlike the 10 and 17 July cases, M1 was already
621 under high aerosol conditions, with particle concentrations consistently elevated at diameters
622 <80 nm. In contrast, S3 remained under low aerosol conditions for most of the day, except for
623 a brief increase just prior to the SBF passage. The SAI did not produce notable changes in
624 aerosol size distribution, bulk chemical composition, or simulated $PM_{2.5}$, indicating that pre-
625 and post-SBF aerosol concentrations were comparable at both sites. Although wind direction
626 changed at M1, the marine-influenced air mass was also burdened by high aerosol loading,
627 limiting its impact on conditions at the site. Similarly, S3 showed no discernible change, with
628 concentrations remaining low before and after the SBF passage. Detailed discussions on these
629 example events will be continued in the next section that expands this discussion to include
630 regional removal and transport influences on these SAI events.

631

632 3.5. Regional influence of sea-breeze aerosol interaction

633 In Fig. 9, we provide the spatial distribution of modeled w , planetary boundary layer height
634 (PBLH), surface-level wind vectors, $PM_{2.5}$, and integrated aerosol number concentration
635 (nucleation-nu0 + accumulation-ac0 mode) using WRF-Chem. Together, nu0 and ac0
636 concentrations reveal size-dependent aerosol changes that bulk $PM_{2.5}$ mass or total number
637 obscure, allowing SBF-driven redistribution to be attributed to specific aerosol modes and
638 clarifying implications for microphysics, CCN/INP, and radiative effects. On 10 July, the
639 observed SBF reached the M1 site at 21:30 UTC and reached the S3 site at 23:45 UTC. The
640 simulation for this event accurately represents this timing for the SBF passage. The output for
641 the time 20:00 UTC on 10 July corresponds to an example point in the simulation and daytime

642 observations when the SBF had not reached either site. The 22:00 UTC examples correspond
643 to a time when the modeled and observed SBF has recently passed the M1 site but not reached
644 the S3 site. The 00:00 UTC examples (next day) correspond to a timing when the SBF has
645 passed both TRACER field sites.

646 Behind the SBF in our simulations, south or southeast winds prevail, passing through from
647 the Gulf of Mexico and blowing onshore at an average speed of 5 m s^{-1} . There is an increase in
648 w associated with the SBF passage. This transition in the air mass is also observed around the
649 M1 site at timestep 22:00 UTC. A similar pattern in the w is observed at the S3 site at the
650 timestep 00:00 UTC. This change at S3 is also accompanied by a decrease in the modeled
651 PBLH.

652 The 10 July simulations help illustrate that while changes in aerosol and meteorological
653 properties are more pronounced near the SBF, SBF influences may extend $>50 \text{ km}$ inland
654 associated with the path and extent of this feature. Along the convergence zone associated with
655 the SBF, particle concentrations are higher ahead of the SBF and lower behind it, due to
656 intrusion of cleaner marine air into the convergence zone. Consequently, SBF passage in the
657 model creates a swath of reduced aerosol concentration (up to 50%) parallel to the Galveston
658 Bay or Gulf of Mexico coastline. Over time, a well-defined dipole pattern emerges,
659 characterized by reduced concentrations over the coastal zone and enhanced concentrations
660 farther inland, consistent with the inland penetration of the maritime air mass and displacement
661 of pre-existing polluted air.

662 The additional example on 17 July (Fig. 10) is suggestive of an enhancement in aerosol
663 concentration associated with the SBF event, while the 16 August event (Fig. 11) is indicative
664 of a neutral influence from the SBF passage. Similar to 10 July, both days exhibit an increase
665 in w associated with passage of the SBF, relative to inland areas not influenced by the front
666 (Figs. 10a, 11a). The SBF passage was also accompanied by a decrease in modeled PBLH
667 (Figs. 10b, 11b). On 17 July, the SBF had reached M1 and S3 by $\sim 19:00$ and $21:00$ UTC,
668 respectively; winds were predominantly from southwest to east, with easterlies likely advecting
669 emissions from the HSC and contributing to the observed enhancements.

670 Notably, the 17 July event occurred in a different ambient aerosol environment than the 10
671 July event. MERRA-2 column dust mass concentrations (Fig. S9) indicate Saharan dust
672 transport on this day, yielding elevated dust loading over the Gulf of Mexico and resulting in

673 marine aerosol mass concentrations that exceeded those over land. The high concentrations are
674 also observed to be more prominent to the southwest of the M1 site (Fig. 10c). Hence, as the
675 SBF moves inland on 17 July, it transports this higher aerosol containing air mass, replacing
676 the lower aerosol containing air over the site and causing an increased aerosol concentration at
677 the M1 site. The onshore winds carry an air mass influenced by both local and long-range
678 transport, originating from both land and sea. In contrast to the other two events, the 16 August
679 event occurred under a transitional regime and likely influenced by the bay breeze. The aerosol
680 environment was notably uniform over the wider regional air masses, thus SBF passage
681 resulted in minimal changes to the aerosol distribution (Fig. 11c, d, f).

682 Overall, one implication from these simulations is that the effect of the inland-
683 penetrating SBF on the aerosol environment appears highly dependent on the pre-existing
684 aerosol condition over the location, as well as the air mass characteristics trailing the SBF. The
685 wind anomaly associated with the Gulf breeze front can transport more (less) polluted, particle-
686 laden air mass, leading to increased (decreased) aerosol concentration as it passes the site
687 during the subsequent ~5 hours after the front passes. A study by Deng et al., (2025) using
688 scanning radar data collected during TRACER reported similar findings during one of the SB
689 events on 10 September 2022. They reported a reduced influence on the aerosol concentration
690 immediately after the passing of the bay breeze front for the next few hours, due to the
691 dominance of onshore flow consistent with the findings from this study (Fig. S2).

692

693 3.6 Sea breeze effects on the vertical distribution of aerosols

694 Fig. 12 shows the modeled normalized $PM_{2.5}$ at different elevations before and after the
695 passage of the SBF. On 10 July, the cleaner marine air mass that follows the SBF led to a
696 decrease in aerosol concentration below 1 km at the ARM sites. The model indicates surface
697 convergence along the SBF (Fig. S10.). The aerosol concentrations are redistributed
698 horizontally and vertically. Two hours later, the SBF reaches the S3 site where its passage
699 causes a similar change in the aerosol concentration. The varying extent of this air mass and its
700 inland propagation redistributes the vertical $PM_{2.5}$ profiles from urban to suburban regions as
701 this SBF moves northwest from Houston. Similar to the changes in the aerosol mass
702 concentrations, the changes in the vertical distributions of ν_0 (Fig. 12b) and ac_0 number
703 concentration (Fig. 12c) are not homogeneous within these layers. The cleaner air mass

704 following the SBF replaces the more polluted continental air, lowering aerosol number
705 concentrations. The response is vertically inhomogeneous, reductions are most prominent
706 around M1 and are strongest below ~500 m. Within the 1.5 km, nu_0 shows the largest negative
707 anomalies (often > 80%) immediately behind the SBF, consistent with marine air being
708 relatively depleted in the smallest particles. A thin narrow yellow/orange area (~+70%
709 normalized changes) behind the front (within 1 to 1.5 km) reflects lifting, which can
710 momentarily concentrate or mix in small particles. The ac_0 exhibits a similar pattern but weaker
711 signal. This reflects that accumulation-mode particles are less sensitive to the front, so the
712 reductions are smaller and less uniform, with occasional localized decreases along the front.
713 Overall, the inland-propagating SBF drives an exchange between cleaner marine and more
714 polluted continental air masses, redistributing aerosols both horizontally and vertically.

715 These results complement those shown in SB simulations by Lu and Turco (1994),
716 Verma et al., (2006), Igel et al., (2018), and Parajuli et al., (2022). Parajuli et al., (2022)
717 observed that the SB pushes dust inland and upward along the mountain slopes, reaching
718 heights of up to 1.5 km. During TRACER, the vertical influence of SAI extended up to ~1.5
719 km (~PBLH). The region of SBC influence is shown to extend inland up to 50 km and vertically
720 up to 2 km over a period of up to 5 hours following the passage of the SBF. The model
721 simulations supplement the observations by filling observational gaps and enabling the
722 extrapolation of findings across a broader regional scale, an endeavor that would be challenging
723 to achieve with limited in-situ observational sites or standalone models.

724

725 3.7 Impacts of sea breeze aerosol interaction on cloud condensation nuclei

726 Fig. 13 shows the time series of the normalized aerosol number concentration with $D_p >$
727 100 nm, N_{100} for the 10 July event. Due to the unavailability of measured CCN data at both M1
728 and S3, N_{100} serves as our proxy for the CCN (CCN proxy) concentration (Ahlm et al., 2013).
729 Hence, the current analysis is limited to observational evidence of N_{100} variability. Similar to
730 the changes in the overall aerosol number budget, the SBF passage and the air mass that follows
731 induces simultaneous changes in the CCN budget. During this event, the CCN proxy
732 concentration decreases by ~35% at the M1 site and ~60% at the S3 site, with these changes
733 observed within an hour of the SBF passage.

Deleted: i

Formatted: Not Superscript/ Subscript

Formatted: Not Superscript/ Subscript

735 Simulations performed for this event also suggest similar changes in aerosol budget,
736 indicating that the SBF brings in a cleaner air mass from directions consistent with a more
737 marine environment. Model results suggest that the CCN concentration at the surface decreases
738 by up to 60%, consistent with the observations. In our supplemental Figs. S11. and S12., we
739 include the temporal variation of the normalized N_{100} during all the other SB events during the
740 TRACER IOP. The preexisting N_{100} is less frequently impacted by the SAI than previous
741 examples we provided for SBF changes to the total number concentration, and these events
742 show a decrease in N_{100} for ~25% of the SB events at both M1 and S3 site. This suggests that
743 the influence of SAI is lesser over the marine influenced regional background aerosol larger
744 than 100 nm in diameter.

745

746 **4 Summary and conclusions**

747 Sea breezes influence multi-scale processes across the land-ocean-atmosphere interface
748 within the region of influence of the SBC. The TRACER field campaign provided a unique
749 opportunity to understand how aerosol and meteorological processes impact weather and
750 climate in the urban and rural coastal environment of Houston, Texas. A total of 46 (M1) and
751 30 (S3) instances of SB passages were identified during the summertime TRACER IOP period.
752 Summertime measurements from the ARM sites coupled with WRF-Chem model simulations
753 (July and August 2022) help to quantify aerosol changes resulting from onshore transport of
754 marine boundary layer air masses due to SBF passage and the associated atmospheric SBC
755 impacts.

756 Understanding the spatial extent and duration of SAIs is crucial for assessing their
757 environmental and meteorological impacts. For inland-penetrating SBFs, aerosol responses fall
758 into one of the three types: reduction (clean marine air replacing more polluted continental air);
759 enhancement (import of more polluted air), or neutral (similar air masses). The sign and
760 magnitude of changes depend on proximity to the coast, the upwind air mass history prior to
761 SBF arrival, and the antecedent airmass aerosol concentrations at each site,

Deleted: coastal

Deleted: and the upwind air mass history prior to SBF arrival...

762 TRACER measurements indicate that the urban M1 site, closer to both Galveston Bay
763 and the Gulf of Mexico, experiences more frequent aerosol concentration changes (increase or
764 decrease during 63% of SB events) than the rural S3 site (increase or decrease during 40% of
765 SB days), which is primarily Gulf-breeze influenced and farther from urban/industrial sources.

769 During IOP events, surface aerosol number changed by up to a factor of two. On average, SBF
770 passages were associated with a decrease of ~23% at M1 and increase of ~4% at S3. SBF
771 passages produce distinct aerosol responses depending on the type of SAI event. At M1,
772 enhancement days (28% of SB events) are associated with an average increase of aerosol
773 concentration by ~55%, while reduction days (35% of SB events) show an average decrease of
774 ~42%. At S3, enhancement days (27% of SB events) exhibit an average increase of ~64%,
775 whereas reduction days (13% of SB events) show a decrease of ~45%.

776 This study also provides support for how SAIs may interfere with aerosol microphysical
777 processes, including NPF events, a key driver of the overall aerosol number budget. These
778 changes occur with sharp meteorological shifts, including RH (+30%) and wind speed (+4 m
779 s⁻¹) increases, and backing to southeasterly flow (Figs. 7. and 8.). The relationship between
780 wind and aerosol number concentrations showed that aerosol concentrations at the M1 site are
781 higher when prevailing winds originate from the direction of the Houston urban core (northwest
782 to north), compared to the winds coming from the sea (south) (Fig. S5). Recently, Rapp et al.
783 (2024) emphasized using targeted mobile sampling that collecting measurements on both sides
784 of SB boundaries are critical for disentangling aerosol from meteorological controls. These
785 findings are complementary to the results in this study that boundary timing and air mass origin
786 drive the different responses at M1 and S3.

787 WRF Chem simulations extend the site perspective regionally, indicating
788 heterogeneous SAI footprints (Figs. 9, 10, 11, and 12). Across 18 simulated events, near surface
789 PM_{2.5} tends to decrease by ~15% around the M1 site and increase by ~3% near the S3 site (Fig.
790 S13). However, these responses vary with altitude (Fig. 12). The SBF may alter the vertical
791 aerosol distribution in the boundary layer up to 2 km. Beyond thermodynamics, SB fronts also
792 reshape convective environments (Wang et al., 2024). [Thermodynamics and air mass across the](#)
793 [maritime and continental sides of these fronts influence storm characteristics and evolution](#)
794 [\(Sharma et al., 2024\)](#).

795 With respect to cloud-relevant particles, both observations and simulations indicate that
796 the surface CCN proxy concentrations decrease by up to 60% following SBF passage (Fig. 13),
797 although such changes are infrequent (~25% of the SB events at both M1 and S3 site), implying
798 a weaker impact of SAI on marine influenced regional background accumulation mode. This
799 aligns with Thompson et al. (2025), which showed that aerosol cloud-forming properties differ
800 between polluted marine and continental air masses, with variability in size, hygroscopicity,

Deleted:)

Deleted: The storm characteristics across maritime vs. continental sides of these fronts drive the air mass contrasts produced by SBCs (Sharma et al., 2024), which can further influence the aerosol environment

806 and CCN efficiency across sites. Given the complex mix of marine, terrestrial, and urban
807 sources, and the strong spatial heterogeneity revealed by both our analysis and prior TRACER
808 studies, future studies should include direct CCN and INP measurements and size-resolved
809 aerosol properties to better capture the role of SAI in aerosol–cloud interactions. It is important
810 to remember that these effects are localized, occurring only during shorter timescales (~5
811 hours) associated with daily SBC cycles over these locations. But these SAI timings align with
812 periods of peak solar radiation and elevated aerosol concentrations, potentially leading to
813 significant impacts on the radiation budget over the coastal regions. During times in close
814 proximity to SBF passage, changes in solar radiation and cloud formation may influence the
815 aerosol formation and distribution, modify atmospheric chemical reactions, and affect cloud
816 formation and properties, thereby impacting various atmospheric processes and interactions.
817 Because many coastal cities have high aerosol loading with frequent SBCs, accounting for SAI
818 when estimating direct aerosol radiative forcing is crucial. However, quantifying these changes
819 is challenging, underscoring the need for detailed future studies across diverse coastal regions.

820

821 **Code and data availability.** DOE-ARM datasets can be downloaded from the ARM data
822 discovery ([#/results/instrument_class_code:##](https://adc.arm.gov//discovery/#/results/instrument_class_code:)). The TCEQ
823 data can be downloaded from <https://www.tceq.texas.gov/agency/data> and [sfcmetradatq-tceq](https://www.sfcmetradatq-tceq.com)
824 ARM PI product (<https://doi.org/10.5439/2587278>) The Weather Research and Forecasting
825 Model with Chemistry model code is available from
826 www2.mmm.ucar.edu/wrf/users/download/. WRF-Chem preprocessors are available on the
827 website (www.aom.ucar.edu/wrf-chem). The model output data is made available upon
828 request. The primary tools to analyze the model output and generate figures are CDO
829 (code.mpimet.mpg.de/projects/cdo/), MATLAB (www.mathworks.com/products/), and
830 Jupyter Notebook platform (<https://jupyter.org>).

831

832 **Supplement.** The supplementary document contains supplementary figures referred to in the
833 main manuscript.

834

835 **Author contribution.** TS and CK planned the study; TS conducted the analysis and wrote the
836 manuscript; MH provided the aerosol data; MJ, MD, SG, MH, AS, DW, MZ and CK reviewed
837 and edited the manuscript.

838

839 **Competing interests.** The authors declare that they have no conflict of interest.

840

841 **Acknowledgments.** We would like to acknowledge support from the Atmospheric System
842 Research (ASR) program, the Atmospheric Radiation Measurement (ARM) user facility, and
843 the ARM TRACER operation and science teams. This research was supported in part by
844 resources provided by the National Energy Research Scientific Computing Center (NERSC),
845 a DOE Office of Science User Facility under Contract No. DE-AC02-05CH11231, through
846 NERSC award BER-ERCAP0026649. Additionally, the NE Linux Cluster (nlc) at Brookhaven
847 National Laboratory was utilized for model simulations and output storage.

848

849 **Financial support.** This paper has been authored by employees of Brookhaven Science
850 Associates, LLC, under Contract DE-SC0012704 with the U.S. Department of Energy (DOE).

851

852

853 **References**

854 Ackermann, I. J., Hass, H., Memmesheimer, M., Ebel, A., Binkowski, F. S., & Shankar, U.:
855 Modal aerosol dynamics model for Europe: Development and first applications.
856 Atmospheric Environment, 32(17), 2981–2999. [https://doi.org/10.1016/S1352-](https://doi.org/10.1016/S1352-2310(98)00006-5)
857 [2310\(98\)00006-5](https://doi.org/10.1016/S1352-2310(98)00006-5), 1998.

858 Adaricheva, K., Bernhardt, J. E., Liu, W., & Schmidt, B.: Importance of overnight parameters
859 to predict Sea Breeze on Long Island. <http://arxiv.org/abs/2309.01803>, 2023.

860 Ahlm, L., Junn, J., Fountoukis, C., Pandis, S. N., & Riipinen, I. (2013). Particle number
861 concentrations over Europe in 2030: The role of emissions and new particle formation.
862 Atmospheric Chemistry and Physics, 13(20), 10271–10283.
863 <https://doi.org/10.5194/acp-13-10271-2013>

864 Ahmadov, R., Gerbig, C., Kretschmer, R., Koerner, S., Neininger, B., Dolman, A. J., & Sarrat,
865 C.: Mesoscale covariance of transport and CO₂ fluxes: Evidence from observations and
866 simulations using the WRF-VPRM coupled atmosphere-biosphere model. *Journal of*
867 *Geophysical Research Atmospheres*, 112(22). <https://doi.org/10.1029/2007JD008552>,
868 2007.

869 Albrecht, B. A.: Aerosols, cloud microphysics, and fractional cloudiness. *Science*, 245, 1227–
870 1230, 1989.

871 Aldhaif, A. M., Lopez, D. H., Dadashazar, H., & Sorooshian, A.: Sources, frequency, and
872 chemical nature of dust events impacting the United States East Coast. *Atmospheric*
873 *Environment*, 231. <https://doi.org/10.1016/j.atmosenv.2020.117456>, 2020.

874 Ariya, P., Sun, J., Eltouny, N., Hudson, E. D., Hayes, C. T., & Kos, G.: Physical and chemical
875 characterization of bioaerosols—Implications for nucleation processes. *International*
876 *Reviews in Physical Chemistry*, 28(1), 1–32.
877 <https://doi.org/10.1080/01442350802597438>, 2009.

878 Arrillaga, J. A., Jiménez, P., de Arellano, J. V.-G., Jiménez, M. A., Román-Cascón, C., Sastre,
879 M., and Yagüe, C.: Analyzing the synoptic-, meso- and local-scale involved in sea
880 breeze formation and frontal characteristics. *J. Geophys. Res. Atmos.*, 125,
881 e2019JD031302, <https://doi.org/10.1029/2019JD031302>, 2020.

882 Atabakhsh, S., Poulain, L., Bigi, A., Coen, M. C., Pöhlker, M., & Herrmann, H.: Trends of
883 PM₁ aerosol chemical composition, carbonaceous aerosol, and source over the last 10
884 years at Melpitz (Germany). *Atmospheric Environment*, 346.
885 <https://doi.org/10.1016/j.atmosenv.2025.121075>, 2025.

886 Augustin, P., Billet, S., Crumeyrolle, S., Deboudt, K., Dieudonné, E., Flament, P., Fourmentin,
887 M., Guilbaud, S., Hanoune, B., Landkocz, Y., Méausoone, C., Roy, S., Schmitt, F. G.,
888 Sentchev, A., & Sokolov, A.: Impact of sea breeze dynamics on atmospheric pollutants
889 and their toxicity in industrial and urban coastal environments. *Remote Sensing*, 12(4).
890 <https://doi.org/10.3390/rs12040648>, 2020.

891 Banta, R. M., Senff, C. J., Alvarez, R. J., Langford, A. O., Parrish, D. D., Trainer, M. K., Darby,
892 L. S., Michael Hardesty, R., Lambeth, B., Andrew Neuman, J., Angevine, W. M.,
893 Nielsen-Gammon, J., Sandberg, S. P., & White, A. B.: Dependence of daily peak O₃
894 concentrations near Houston, Texas on environmental factors: Wind speed,

895 temperature, and boundary-layer depth. *Atmospheric Environment*, 45(1), 162–173.
896 <https://doi.org/10.1016/j.atmosenv.2010.09.030>, 2011.

897 Bao, S., Pietrafesa, L., Gayes, P., Noble, S., Viner, B., Qian, J. H., Werth, D., Mitchell, G., &
898 Burdette, S.: Mapping the Spatial Footprint of Sea Breeze Winds in the Southeastern
899 United States. *Journal of Geophysical Research: Atmospheres*, 128(7).
900 <https://doi.org/10.1029/2022JD037524>, 2023.

901 Barrett, T. E., & Sheesley, R. J.: Urban impacts on regional carbonaceous aerosols: Case study
902 in central Texas. *Journal of the Air and Waste Management Association*, 64(8), 917–
903 926. <https://doi.org/10.1080/10962247.2014.904252>, 2014.

904 Bauman, W. H.: Verify MesoNAM Performance. NASA Contractor Report CR-2010-216-287,
905 Kennedy Space Center, FL, 31 pp. [Available from ENSCO, Inc., 1980 N. Atlantic
906 Ave., Suite 830, Cocoa Beach, FL, 32931 and online at
907 <http://science.ksc.nasa.gov/amu/final-reports/mesoNAMverify.pdf>.], 2010.

908 Bond, T. C., Doherty, S. J., Fahey, D. W., Forster, P. M., Berntsen, T., Deangelo, B. J., Flanner,
909 M. G., Ghan, S., Kärcher, B., Koch, D., Kinne, S., Kondo, Y., Quinn, P. K., Sarofim,
910 M. C., Schultz, M. G., Schulz, M., Venkataraman, C., Zhang, H., Zhang, S., ... Zender,
911 C. S.: Bounding the role of black carbon in the climate system: A scientific assessment.
912 *Journal of Geophysical Research Atmospheres*, 118(11), 5380–5552.
913 <https://doi.org/10.1002/jgrd.50171>, 2013.

914 Borge, R., Alexandrov, V., José del Vas, J., Lumbreras, J., & Rodríguez, E.: A comprehensive
915 sensitivity analysis of the WRF model for air quality applications over the Iberian
916 Peninsula. *Atmospheric Environment*, 42(37), 8560–8574.
917 <https://doi.org/10.1016/j.atmosenv.2008.08.032>, 2008.

918 Boyer, C. H., Keeler, J. M., & Rakoczy, B. C. (2025). An Idealized Parameter Study of
919 Destabilization and Convection Initiation in Coastal Regions. Part I: Calm or Offshore
920 Synoptic-Scale Flow. *Journal of the Atmospheric Sciences*, 82(3), 519–539.
921 <https://doi.org/10.1175/JAS-D-23-0180.1>

922 Boyouk, N., Léon, J. F., Delbarre, H., Augustin, P., & Fourmentin, M.: Impact of sea breeze
923 on vertical structure of aerosol optical properties in Dunkerque, France. *Atmospheric
924 Research*, 101(4), 902–910. <https://doi.org/10.1016/j.atmosres.2011.05.016>, 2011.

- 925 Bozlaker, A., Prospero, J. M., Fraser, M. P., & Chellam, S.: Quantifying the contribution of
926 long-range saharan dust transport on particulate matter concentrations in Houston,
927 Texas, using detailed elemental analysis. *Environmental Science and Technology*,
928 47(18), 10179–10187. <https://doi.org/10.1021/es4015663>, 2013.
- 929 Brown, S., Nicholls, R. J., Woodroffe, C. D., Hanson, S., Hinkel, J., Kebede, A. S., Neumann,
930 B. and Vafeidis, A. T.: “Sea-Level Rise Impacts and Responses: A Global Perspective.”
931 In *Coastal Hazards*, edited by Charles W. Finkl, 117–49. Dordrecht: Springer
932 Netherlands. https://doi.org/10.1007/978-94-007-5234-4_5, 2013.
- 933 Burkart, J., Gratzl, J., Seifried, T. M., Bieber, P., & Grothe, H.: Subpollen particles (SPP) of
934 birch as carriers of ice nucleating macromolecules. *Biogeosciences Discussions*, 1–15,
935 2021.
- 936 Charlson, R. J., Schwartz, S. E., Hales, J. M., Cess, R. D., Coakley, J. A. Jr, Hansen, J. E., and
937 Hofmann, D. J.: Climate forcing by anthropogenic aerosols. *Science* 255, 423–430,
938 1992.
- 939 Chen, F., & Dudhia, J.: Coupling an advanced land surface-hydrology model with the Penn
940 State-NCAR MM5 modeling system. Part I: Model implementation and sensitivity.
941 *Monthly Weather Review*, 129(4), 569–585. [https://doi.org/10.1175/1520-
942 0493\(2001\)129<0569:caalsh>2.0.co;2](https://doi.org/10.1175/1520-0493(2001)129<0569:caalsh>2.0.co;2), 2001.
- 943 Chou, M., Suarez, M. J., Ho, C., Yan, M. M., & Lee, K.: Parameterizations for cloud
944 overlapping and shortwave single-scattering properties for use in general circulation
945 and cloud ensemble models. *Journal of Climate*, 11(2), 202–214. [https://doi.
946 org/10.1175/1520-0442\(1998\)011<0202:PFCOAS>2.0.CO;2](https://doi.org/10.1175/1520-0442(1998)011<0202:PFCOAS>2.0.CO;2), 1998.
- 947 Clappier, A., Martilli, A., Grossi, P., Thunis, P., Pasi, F., Krueger, B. C., Calpini, B., &
948 Graziani, G., Bergh, H.V.D.: Effect of Sea Breeze on Air Pollution in the Greater
949 Athens Area. Part I: Numerical Simulations and Field Observations. *J. of Applied
950 meteorology*, (39). [https://doi.org/10.1175/1520-
951 0450\(2000\)039<0546:EOSBOA>2.0.CO;2](https://doi.org/10.1175/1520-0450(2000)039<0546:EOSBOA>2.0.CO;2), 1999.
- 952 Comin, A. N., Miglietta, M. M., Rizza, U., Acevedo, O. C., & Degrazia, G. A.: Investigation
953 of sea-breeze convergence in Salento Peninsula (southeastern Italy). *Atmospheric
954 Research*, 160, 68–79. <https://doi.org/10.1016/j.atmosres.2015.03.010>, 2015.

955 Crippa, M., Canonaco, F., Lanz, V. A., Äijälä, M., Allan, J. D., Carbone, S., Capes, G.,
956 Ceburnis, D., Dall'Osto, M., Day, D. A., DeCarlo, P. F., Ehn, M., Eriksson, A., Freney,
957 E., Hildebrandt Ruiz, L., Hillamo, R., Jimenez, J. L., Junninen, H., KiendlerScharr, A.,
958 Kortelainen, A. M., Kulmala, M., Laaksonen, A., Mensah, A. A., Mohr, C., Nemitz, E.,
959 O'Dowd, C., Ovadnevaite, J., Pandis, S. N., Petäjä, T., Poulain, L., Saarikoski, S.,
960 Sellegri, K., Swietlicki, E., Tiitta, P., Worsnop, D. R., Baltensperger, U., Prévôt, A. S.
961 H.: Organic aerosol components derived from 25 AMS data sets across Europe using a
962 consistent ME-2 based source apportionment approach. *Atmos. Chem. Phys.* 14 (12),
963 6159–6176. <https://doi.org/10.5194/acp-14-6159, 2014>.

964 Crossett, K., Culliton, T., Wiley, P., & Goodspeed, T.: Population trends along the coastal
965 United States, 1980–2008. Silver Spring, National Oceanic and Atmospheric
966 Administration, 2004.

967 Das, S., Prospero, J. M., & Chellam, S.: Quantifying international and interstate contributions
968 to primary ambient PM_{2.5} and PM₁₀ in a complex metropolitan atmosphere.
969 *Atmospheric Environment*, 292. [https://doi.org/10.1016/j.atmosenv.2022.119415,](https://doi.org/10.1016/j.atmosenv.2022.119415, 2023)
970 2023.

971 Deng, Min, et al.: A Closed Bay-Breeze Circulation and Its Lifecycle from TRACER with a
972 New Orienteering Tape Recorder Diagram, *Journal of Geophysical Research:*
973 *Atmospheres* (under revision), 2025.

974 di Bernardino, A., Iannarelli, A. M., Casadio, S., Mevi, G., Campanelli, M., Casasanta, G.,
975 Cede, A., Tiefengraber, M., Siani, A. M., Spinei, E., & Cacciani, M.: On the effect of
976 sea breeze regime on aerosols and gases properties in the urban area of Rome, Italy.
977 *Urban Climate*, 37. <https://doi.org/10.1016/j.uclim.2021.100842, 2021>.

978 Emmons, L. K., Walters, S., Hess, P. G., Lamarque, J. F., Pfister, G. G., Fillmore, D., et al.:
979 Description and evaluation of the model for ozone and related chemical tracers, version
980 4 (MOZART-4). *Geoscientific Model Development*, 3(1), 43–67.
981 <https://doi.org/10.5194/gmd-3-43-2010, 2010>.

982 Dueker, M. E., O'Mullan, G. D., Martínez, J. M., Juhl, A. R., & Weathers, K. C.: Onshore
983 wind speed modulates microbial aerosols along an urban waterfront. *Atmosphere*,
984 8(11). <https://doi.org/10.3390/atmos8110215, 2017>.

985 Fang, C., Li, X., Li, J., Tian, J., & Wang, J. (2025). Research on the impact of land use and
986 land cover changes on local meteorological conditions and surface ozone in the north
987 China plain from 2001 to 2020. *Scientific Reports*, 15(1).
988 <https://doi.org/10.1038/s41598-025-85940-0>

989 Gangoiti, G., Millán, M. M., Salvador, R., & Mantilla, E.: Long-range transport and re-
990 circulation of pollutants in the western Mediterranean during the project Regional
991 Cycles of Air Pollution in the West-Central Mediterranean Area. *Atmospheric*
992 *Environment*, 35(36), 6267–6276. [https://doi.org/10.1016/S1352-2310\(01\)00440-X](https://doi.org/10.1016/S1352-2310(01)00440-X),
993 2001.

994 Gelaro, R., and Coauthors: The Modern-Era Retrospective Analysis for Research and
995 Applications, version 2 (MERRA-2). *J. Climate*, 30, 5419–5454,
996 <https://doi.org/10.1175/JCLI-D-16-0758.1>, 2017.

997 Georgiou, G. K., Christoudias, T., Proestos, Y., Kushta, J., Pikridas, M., Sciare, J., Savvides,
998 C., & Lelieveld, J.: Evaluation of WRF-Chem model (v3.9.1.1) real-Time air quality
999 forecasts over the Eastern Mediterranean. *Geoscientific Model Development*, 15(10),
1000 4129–4146. <https://doi.org/10.5194/gmd-15-4129-2022>, 2022.

1001 Gettelman, A., Mills, M. J., Kinnison, D. E., Garcia, R. R., Smith, A. K., Marsh, D. R., et al.:
1002 The wholeatmosphere community climate modelversion 6 (WACCM6). *Journal of*
1003 *Geophysical Research: Atmospheres*, 124, <https://doi.org/10.1029/2019JD030943>,
1004 2019.

1005 Glantz, P., Nilsson, D. E., & von Hoyningen-Huene, W. (2006). Estimating a relationship
1006 between aerosol optical thickness and surface wind speed over the ocean. In *Atmos.*
1007 *Chem. Phys. Discuss (Vol. 6)*. www.atmos-chem-phys-discuss.net/6/11621/2006/

1008 Grell, G. A., & Devenyi, D.: A generalized approach to parameterizing convection combining
1009 ensemble and data assimilation techniques. *Geophysical Research Letters*, 29(4), 38-1–
1010 38-4. <https://doi.org/10.1029/2002GL015311>, 2002.

1011 Grell, G. A., Peckham, S. E., Schmitz, R., McKeen, S. A., Frost, G., Skamarock, W. C., &
1012 Eder, B.: Fully coupled “online” chemistry within the WRF model. *Atmospheric*
1013 *Environment*, 39(37), 6957–6975. <https://doi.org/10.1016/j.atmosenv.2005.04.027>,
1014 2005.

- 1015 Guenther, A. B., Jiang, X., Heald, C. L., Sakulyanontvittaya, T., Duhl, T., Emmons, L. K., &
1016 Wang, X.: The model of emissions of gases and aerosols from nature version 2.1
1017 (MEGAN2.1): An extended and updated framework for modeling biogenic emissions.
1018 *Geoscientific Model Development*, 5(6), 1471–1492. [https://doi.org/10.5194/gmd-5-](https://doi.org/10.5194/gmd-5-1471-2012)
1019 1471-2012, 2012.
- 1020 Hanft, W., & Houston, A. L.: An Observational and Modeling Study of Mesoscale Air Masses
1021 with High Theta-E. <https://doi.org/10.1175/MWR-D-17, 2018>.
- 1022 Hernández-Ceballos, M. A., Sorribas, M., San Miguel, E. G., Cinelli, G., Adame, J. A., &
1023 Bolívar, J. P.: Impact of sea-land breezes on 210Pb in southern Iberian Peninsula–
1024 Feasibility study on using submicron-sized aerosol particles to analyze 210Pb hourly
1025 patterns. *Atmospheric Pollution Research*, 7(1), 1–8.
1026 <https://doi.org/10.1016/j.apr.2015.06.011>, 2016.
- 1027 Hong, S. Y., Noh, Y., & Dudhia, J.: A new vertical diffusion package with an explicit treatment
1028 of entrainment processes. *Monthly Weather Review*, 134(9), 2318–2341.
1029 <https://doi.org/10.1175/MWR3199.1, 2006>.
- 1030 Hu, L. (2021). A Global Assessment of Coastal Marine Heatwaves and Their Relation With
1031 Coastal Urban Thermal Changes. *Geophysical Research Letters*, 48(9).
1032 <https://doi.org/10.1029/2021GL093260>
- 1033 Huang, X. F., He, L. Y., Hu, M., Canagaratna, M. R., Sun, Y., Zhang, Q., Zhu, T., Xue, L.,
1034 Zeng, L. W., Liu, X. G., Zhang, Y. H., Jayne, J. T., Ng, N. L., Worsnop, D. R.: Highly
1035 time-resolved chemical characterization of atmospheric submicron particles during
1036 2008 Beijing Olympic Games using an Aerodyne High-Resolution Aerosol Mass
1037 Spectrometer. *Atmos. Chem. Phys.* 2010, 10, 8933–8945, DOI: 10.5194/acp-10-8933-
1038 2010.
- 1039 Hudson, B.: Coastal Land Loss and the Mitigation-Adaptation Dilemma: Between Scylla and
1040 Charybdis Repository Citation Coastal Land Loss and the Mitigation-Adaptation
1041 Dilemma: Between Scylla and Charybdis. In *Louisiana Law Review* (Vol. 73).
1042 <https://digitalcommons.law.lsu.edu/lalrev/vol73/iss1/3, 2012>.
- 1043 Igel, A. L., van den Heever, S. C., & Johnson, J. S.: Meteorological and Land Surface
1044 Properties Impacting Sea Breeze Extent and Aerosol Distribution in a Dry

1045 Environment. *Journal of Geophysical Research: Atmospheres*, 123(1), 22–37.
1046 <https://doi.org/10.1002/2017JD027339>, 2018.

1047 IPCC, Intergovernmental Panel on Climate Change: In V. Masson-Delmotte, P. Zhai, A.
1048 Pirani, S. L. Connors, C. P. An, S. Berger, et al. (Eds.), *The Physical Science Basis.*
1049 *Contribution of Working Group I to the Sixth Assessment Report of the*
1050 *Intergovernmental Panel on Climate Change.* Cambridge University Press.
1051 <https://doi.org/10.1017/9781009157896>, 2021.

1052 Iwai, H., Murayama, Y., Ishii, S., Mizutani, K., Ohno, Y., & Hashiguchi, T.: Strong Updraft at
1053 a Sea-Breeze Front and Associated Vertical Transport of Near-Surface Dense Aerosol
1054 Observed by Doppler Lidar and Ceilometer. *Boundary-Layer Meteorology*, 141(1),
1055 117–142. <https://doi.org/10.1007/s10546-011-9635-z>, 2011.

1056 Janjic, Z. I.: Nonsingular implementation of the Mellor–Yamada level 2.5 scheme in the NCEP
1057 Meso model. NCEP Office Note, 437, 61, 2002.

1058 Jensen, M. P., and Coauthors, (2022): A Succession of Cloud, Precipitation, Aerosol, and Air
1059 Quality Field Experiments in the Coastal Urban Environment. *Bull. Amer. Meteor.*
1060 *Soc.*, 103, 103–105, <https://doi.org/10.1175/BAMS-D-21-0104.1>, 2022.

1061 Jensen, M. P., Flynn, J. H., Gonzalez-Cruz, J. E., Judd, L. M., Kollias, P., Kuang, C.,
1062 McFarquhar, G. M., Powers, H., Ramamurthy, P., Sullivan, J., Aiken, A. C., Alvarez,
1063 S. L., Argay, P., Argrow, B., Bell, T. M., Boyer, D., Brooks, S. D., Bruning, E. C.,
1064 Brunner, K., ... Zhu, Z. (2025). Studying Aerosol, Clouds, and Air Quality in the
1065 Coastal Urban Environment of Southeastern Texas. *Bulletin of the American*
1066 *Meteorological Society*. <https://doi.org/10.1175/bams-d-23-0331.1>

1067 Karnae, S., & John, K.: Source apportionment of PM_{2.5} measured in South Texas near U.S.A.
1068 – Mexico border. *Atmospheric Pollution Research*, 10(5), 1663–1676.
1069 <https://doi.org/10.1016/j.apr.2019.06.007>

1070 [Kasparoglu, S., Meskhidze, N., & Petters, M. D. \(2024\). Aerosol mixing state, new particle](https://doi.org/10.1016/j.scitotenv.2024.175307)
1071 [formation, and cloud droplet number concentration in an urban environment. *Science*](https://doi.org/10.1016/j.scitotenv.2024.175307)
1072 [of the Total Environment, 951. <https://doi.org/10.1016/j.scitotenv.2024.175307>](https://doi.org/10.1016/j.scitotenv.2024.175307)

1073 Kerminen, V. M., Chen, X., Vakkari, V., Petäjä, T., Kulmala, M., & Bianchi, F. : Atmospheric
1074 new particle formation and growth: Review of field observations. In *Environmental*

1075 Research Letters (Vol. 13, Issue 10). Institute of Physics Publishing.
1076 <https://doi.org/10.1088/1748-9326/aadf3c>, 2018.

1077 Kgabi, N. A., & Mokgwetsi, T. (2009). Dilution and dispersion of inhalable particulate matter.
1078 WIT Transactions on Ecology and the Environment, 127, 229–238.
1079 <https://doi.org/10.2495/RAV090201>

1080 Kleinman, L. I., Daum, P. H., Imre, D. G., Lee, Y.-N., Nunnermacker, L. J., Springston, S. R.,
1081 Weinstein-Lloyd, J., and Rudolph, J.: Ozone production rate and hydrocarbon reactivity
1082 in 5 urban areas: A cause of high ozone concentration in Houston, Geophys. Res. Lett.,
1083 29(10), 1467, doi:10.1029/2001GL014569, 2002.

1084 Kuang, C., Chen, M., Zhao, J., Smith, J., McMurry, P. H., & Wang, J.: Size and time-resolved
1085 growth rate measurements of 1 to 5 nm freshly formed atmospheric nuclei. Atmospheric
1086 Chemistry and Physics, 12(7), 3573–3589. <https://doi.org/10.5194/acp-12-3573-2012>,
1087 2012.

1088 Kuang, C., McMurry, P. H., and McCormick, A. V.: Determination of cloud condensation
1089 nuclei production from measured new particle formation events, Geophys. Res. Lett.,
1090 36, L09822, doi:10.1029/2009GL037584, 2009.

1091 Kulmala, M., Laakso, L., Lehtinen, K. E. J., Riipinen, I., Dal Maso, M., Anttila, T., Kerminen,
1092 V.-M., Horrak, U., Vana, M., and Tammet, H.: Initial steps of aerosol growth, Atmos.
1093 Chem. Phys., 4, 2553–2560, doi:10.5194/acp-4-2553-2004, 2004.

1094 Kulmala, M., Petäjä, T., Ehn, M., Thornton, J., Sipilä, M., Worsnop, D. R., & Kerminen, V.
1095 M.: Chemistry of atmospheric nucleation: On the recent advances on precursor
1096 characterization and atmospheric cluster composition in connection with atmospheric
1097 new particle formation. Annual Review of Physical Chemistry, 65, 21–37.
1098 <https://doi.org/10.1146/annurev-physchem-040412-110014>, 2014.

1099 Levy, M. E., Zhang, R., Khalizov, A. F., Zheng, J., Collins, D. R., Glen, C. R., Wang, Y., Yu,
1100 X. Y., Luke, W., Jayne, J. T., & Olaguer, E.: Measurements of submicron aerosols in
1101 Houston, Texas during the 2009 SHARP field campaign. Journal of Geophysical
1102 Research Atmospheres, 118(18), 10,518-10,534. <https://doi.org/10.1002/jgrd.50785>,
1103 2013.

1104 Li, W., Wang, Y., Bernier, C., & Estes, M.: Identification of Sea Breeze Recirculation and Its
1105 Effects on Ozone in Houston, TX, During DISCOVER-AQ 2013. *Journal of*
1106 *Geophysical Research: Atmospheres*, 125(22). <https://doi.org/10.1029/2020JD033165>,
1107 2020.

1108 Linden, P.F., Simpson, J.E., Gravity-driven flows in a turbulent fluid. *Journal of Fluid*
1109 *Mechanics*, 172, 481-497. doi:10.1017/S0022112086001829, 1986.

1110 Liu, H., Zhang, B., Moore, R. H., Ziemba, L. D., Ferrare, R. A., Choi, H., Sorooshian, A.,
1111 Painemal, D., Wang, H., Shook, M. A., Scarino, A. J., Hair, J. W., Crosbie, E. C., Fenn,
1112 M. A., Shingler, T. J., Hostetler, C. A., Chen, G., Kleb, M. M., Luo, G., ... Johnson,
1113 M. S.: Tropospheric aerosols over the western North Atlantic Ocean during the winter
1114 and summer deployments of ACTIVATE 2020: Life cycle, transport, and distribution.
1115 *Atmospheric Chemistry and Physics*, 25(4), 2087–2121. [https://doi.org/10.5194/acp-](https://doi.org/10.5194/acp-25-2087-2025)
1116 [25-2087-2025](https://doi.org/10.5194/acp-25-2087-2025), 2025.

1117 Lu, R., & Turco, R. P.: Air pollutant transport in a coastal environment.1. 2-dimensional
1118 simulations of sea-breeze and mountain effects. *Journal of the Atmospheric Sciences*,
1119 51(15), 2285–2308. [https://doi.org/10.1175/1520-](https://doi.org/10.1175/1520-0469(1994)051<2285:APTAC>2.0.CO;2)
1120 [0469\(1994\)051<2285:APTAC>2.0.CO;2](https://doi.org/10.1175/1520-0469(1994)051<2285:APTAC>2.0.CO;2), 1994.

1121 Ma, S., & Tong, D. Q.: Neighborhood Emission Mapping Operation (NEMO): A 1-km
1122 anthropogenic emission dataset in the United States. *Scientific Data*, 9(1).
1123 <https://doi.org/10.1038/s41597-022-01790-9>, 2022.

1124 Mack, S. M., Madl, A. K., & Pinkerton, K. E.: Respiratory health effects of exposure to ambient
1125 particulate matter and bioaerosols. *Comprehensive Physiology*, 10(1), 1–20.
1126 <https://doi.org/10.1002/cphy.c180040>, 2020.

1127 Mao, F., Zang, L., Wang, Z., Pan, Z., Zhu, B., & Gong, W.: Dominant synoptic patterns during
1128 wintertime and their impacts on aerosol pollution in Central China. *Atmospheric*
1129 *Research*, 232. <https://doi.org/10.1016/j.atmosres.2019.104701>, 2020.

1130 Maria, V. D., Rahman, M., Collins, P., Dondi, G., & Sangiorgi, C. (2013). Urban Heat Island
1131 Effect: Thermal Response from Different Types of Exposed Paved Surfaces.
1132 *International Journal of Pavement Research and Technology*, 6(4), 414-422.
1133 [https://doi.org/10.6135/ijprt.org.tw/2013.6\(4\).414](https://doi.org/10.6135/ijprt.org.tw/2013.6(4).414)

- 1134 Masselink, G., and Pattiaratchi, C. B.: The effect of sea breeze on beach morphology, surf zone
1135 hydrodynamics and sediment resuspension, *Mar. Geol.*, 146, 115–135, 1998.
- 1136 Mather, J. H., and Voyles, J. W.: The Arm Climate Research Facility: A Review of Structure
1137 and Capabilities. *Bull. Amer. Meteor. Soc.*, 94, 377–392,
1138 <https://doi.org/10.1175/BAMS-D-11-00218.1>, 2013.
- 1139 Miller, S. T. K., Keim, B. D., Talbot, R. W., & Mao, H.: Sea breeze: Structure, forecasting,
1140 and impacts. *Reviews of Geophysics*, 41(3). <https://doi.org/10.1029/2003RG000124>,
1141 2003.
- 1142 Minguillón, M. C., Ripoll, A., Pérez, N., Prévôt, A. S. H., Canonaco, F., Querol, X., and
1143 Alastuey, A.: Chemical characterization of submicron regional background aerosols in
1144 the western Mediterranean using an Aerosol Chemical Speciation Monitor, *Atmos.*
1145 *Chem. Phys.*, 15, 6379–6391, <https://doi.org/10.5194/acp-15-6379-2015>, 2015.
- 1146 Mlawer, E. J., Taubman, S. J., Brown, P. D., Iacono, M., & Clough, S. A.: Radiative transfer
1147 for inhomogeneous atmospheres: RRTM, a validated correlated-k model for the
1148 longwave. *Journal of Geophysical Research*, 102(D14), 16663–16682.
1149 <https://doi.org/10.1029/97JD00237>, 1997.
- 1150 Monin, A. S., & Obukhov, A. M.: Basic laws of turbulent mixing in the surface layer of the
1151 atmosphere. *Contributions of the Geophysical Institute of the Slovak Academy of*
1152 *Science, USSR*, 151, 163–187, 1954.
- 1153 Moorthy, K. K., Murthy, B. V. K., and Nair, P. R.: Sea-breeze front effects on boundary layer
1154 aerosols at a tropical station, *J. Appl. Meteorol.*, 32, 1196–1205. 1993.
- 1155 Moorthy, K. K., Pillai, P. S., & Suresh Babu, S.: Influence of changes in the prevailing synoptic
1156 conditions on the response of aerosol characteristics to land-and sea-breeze circulations
1157 at a coastal station. In *Boundary-Layer Meteorology (Vol. 108)*, 2003.
- 1158 Morrison, H., Curry, J. A., and Khvorostyanov, V. I.: A new double-moment microphysics
1159 parameterization for application in cloud and climate models. Part I: Description.
1160 *Journal of the Atmospheric Sciences*, 62(6), 1665–1677.
1161 <https://doi.org/10.1175/jas3446.1>, 2005.

- 1162 Papanastasiou, D. K., Melas, D., Bartzanas, T., & Kittas, C.: Temperature, comfort and
1163 pollution levels during heat waves and the role of sea breeze. *International Journal of*
1164 *Biometeorology*, 54(3), 307–317. <https://doi.org/10.1007/s00484-009-0281-9>, 2010.
- 1165 Parajuli, S. P., Stenchikov, G. L., Ukhov, A., Mostamandi, S., Kucera, P. A., Axisa, D.,
1166 Gustafson, W. I., & Zhu, Y.: Effect of dust on rainfall over the Red Sea coast based on
1167 WRF-Chem model simulations. *Atmospheric Chemistry and Physics*, 22(13), 8659–
1168 8682. <https://doi.org/10.5194/acp-22-8659-2022>, 2022.
- 1169 Parajuli, S., Stenchikov, G. G., Ukhov, A., Shevchenko, I., Dubovik, O., & Lopatin, A.:
1170 Aerosol vertical distribution and interactions with land/sea breezes over the eastern
1171 coast of the Red Sea from lidar data and high-resolution WRF-Chem simulations.
1172 *Atmospheric Chemistry and Physics*, 20(24), 16089–16116.
1173 <https://doi.org/10.5194/acp-20-16089-2020>, 2020.
- 1174 Park, J. M., van den Heever, S. C., Igel, A. L., Grant, L. D., Johnson, J. S., Saleeby, S. M.,
1175 Miller, S. D., & Reid, J. S. (2020). Environmental Controls on Tropical Sea Breeze
1176 Convection and Resulting Aerosol Redistribution. *Journal of Geophysical Research:*
1177 *Atmospheres*, 125(6). <https://doi.org/10.1029/2019JD031699>, 2020.
- 1178 Park, M. J., and van den Heever, S. C.: Weakening of tropical sea breeze convective systems
1179 through interactions of aerosol, radiation, and soil moisture. *Atmospheric Chemistry*
1180 *and Physics*, 22(16), 10527–10549. <https://doi.org/10.5194/acp-22-10527-2022>, 2022.
- 1181 Parrish, D. D., Allen, D. T., Bates, T. S., Estes, M., Fehsenfeld, F. C., Feingold, G., Ferrare,
1182 R., Hardesty, R. M., Meagher, J. F., Nielsen-Gammon, J. W., Pierce, R. B., Ryerson,
1183 T. B., Seinfeld, J. H., & Williams, E. J.: Overview of the second texas air quality study
1184 (TexAQS II) and the Gulf of Mexico atmospheric composition and climate study
1185 (GoMACCS). *Journal of Geophysical Research Atmospheres*, 114(13).
1186 <https://doi.org/10.1029/2009JD011842>, 2009.
- 1187 Partanen, A. I., Landry, J. S., and Matthews, H. D.: Climate and health implications of future
1188 aerosol emission scenarios. *Environmental Research Letters*, 13(2).
1189 <https://doi.org/10.1088/1748-9326/aaa511>, 2018.
- 1190 Perry, K. D., Cahill, T. A., Eldred, R. A., Dutcher, D. D., and Gill, T. E.: Long-range transport
1191 of North African dust to the eastern United States. *Journal of Geophysical Research*
1192 *Atmospheres*, 102(10), 11225–11238. <https://doi.org/10.1029/97jd00260>, 1997.

1193 Pinto, J. P., Dibb, J., Lee, B. H., Rappenglück, B., Wood, E. C., Levy, M., Zhang, R. Y., Lefer,
1194 B., Ren, X. R., Stutz, J., Tsai, C., Ackermann, L., Golovko, J., Herndon, S. C., Oakes,
1195 M., Meng, Q. Y., Munger, J. W., Zahniser, M., & Zheng, J.: Intercomparison of field
1196 measurements of nitrous acid (HONO) during the SHARP campaign. *Journal of*
1197 *Geophysical Research*, 119(9), 5583–5601. <https://doi.org/10.1002/2013JD020287>,
1198 2014.

1199 Plant, R. S., & Keith, G. J.: Occurrence of Kelvin-Helmholtz billows in sea-breeze circulations.
1200 *Boundary-Layer Meteorology*, 122(1), 1–15. [https://doi.org/10.1007/s10546-006-](https://doi.org/10.1007/s10546-006-9089-x)
1201 9089-x, 2007.

1202 Qi, L., Vogel, A. L., Esmailirad, S., Cao, L., Zheng, J., Jaffrezo, J. L., Fermo, P., Kasper-
1203 Giebl, A., Daellenbach, K. R., Chen, M., Ge, X., Baltensperger, U., Prévôt, A. S. H., &
1204 Slowik, J. G.: A 1-year characterization of organic aerosol composition and sources
1205 using an extractive electrospray ionization time-of-flight mass spectrometer (EESI-
1206 TOF). *Atmospheric Chemistry and Physics*, 20(13), 7875–7893.
1207 <https://doi.org/10.5194/acp-20-7875-2020>, 2020.

1208 Ramanathan, V., Crutzen, P. J., Kiehl, J. T., & Rosenfeld, D.: Aerosols, Climate, and the
1209 Hydrological Cycle. *Science*, 294, 5549, DOI: 10.1126/science.1064034, 2001.

1210 Rao, P. A., & Fuelberg, H. E.: An Investigation of Convection behind the Cape Canaveral Sea-
1211 Breeze Front, 2000.

1212 Rapp, A. D., Brooks, S. D., Nowotarski, C. J., Sharma, M., Thompson, S. A., Chen, B., et al.
1213 (2024). TAMU TRACER: Targeted mobile measurements to isolate the impacts of
1214 aerosols and meteorology on deep convection. *Bulletin of the American Meteorological*
1215 *Society*, 105(9), E1685–E1702. <https://doi.org/10.1175/BAMS-D-23-0218.1>

1216 Rodier, Q., Masson, V., Couvreux, F., & Paci, A. (2017). Evaluation of a buoyancy and shear
1217 based mixing length for a turbulence scheme. *Frontiers in Earth Science*, 5.
1218 <https://doi.org/10.3389/feart.2017.00065>

1219 Rosenfeld, D., et al.: Flood or drought: How do aerosols affect precipitation? *Science*, 321,
1220 1309–1313, 2008.

1221 Ryerson, T. B., Trainer, M., Angevine, W. M., Brock, C. A., Dissly, R. W., Fehsenfeld, F. C.,
1222 Frost, G. J., Goldan, P. D., Holloway, J. S., Hübler, G., Jakoubek, R. O., Kuster, W. C.,

1223 Neuman, J. A., Nicks, D. K., Parrish, D. D., Roberts, J. M., Sueper, D. T., Atlas, E. L.,
1224 Donnelly, S. G., et al.: Effect of petrochemical industrial emissions of reactive alkenes
1225 and NO_x on tropospheric ozone formation in Houston, Texas. *Journal of Geophysical*
1226 *Research: Atmospheres*, 108(8). <https://doi.org/10.1029/2002jd003070>, 2003.

1227 Schell, B., Ackerman, I. J., Hass, H., Binkowski, F. S., & Ebel, A.: Modelling the formation
1228 of secondary organic aerosol within a comprehensive air quality model system. *Journal*
1229 *of Geophysical Research*, 106(D22), 28275–28293.
1230 <https://doi.org/10.1029/2001JD000384>, 2001.

1231 Seinfeld, J.H.; Pandis, S.N. *Atmospheric Chemistry and Physics: From Air Pollution to*
1232 *Climate Change*, 2nd ed.; Wiley: Hoboken, NJ, USA, 2006.

1233 Sharma, M., Rapp, A. D., Nowotarski, C. J., & Brooks, S. D. (2024). Observed Variability in
1234 Convective Cell Characteristics and Near-Storm Environments across the Sea- and
1235 Bay-Breeze Fronts in Southeast Texas. *Monthly Weather Review*, 152(11), 2419–2441.
1236 <https://doi.org/10.1175/MWR-D-23-0243.1>

1237 Shrestha, S., Zhou, S., Mehra, M., Guagenti, M., Yoon, S., Alvarez, S. L., Guo, F., Chao, C.
1238 Y., Flynn, J. H., Wang, Y., Griffin, R. J., Usenko, S., & Sheesley, R. J.: Evaluation of
1239 aerosol- and gas-phase tracers for identification of transported biomass burning
1240 emissions in an industrially influenced location in Texas, USA. *Atmospheric Chemistry*
1241 *and Physics*, 23(19), 10845–10867. <https://doi.org/10.5194/acp-23-10845-2023>, 2023.

1242 Shrivastava, M., Zhang, J., Zaveri, R. A., Zhao, B., Pierce, J. R., O'Donnell, S. E., et al.:
1243 Anthropogenic extremely low volatility organics (ELVOCs) govern the growth of
1244 molecular clusters over the Southern Great Plains during the springtime. *Journal of*
1245 *Geophysical Research: Atmospheres*, 129, e2024JD041212,
1246 <https://doi.org/10.1029/2024JD041212>, 2024.

1247 Simpson, J. E.: *Sea Breeze and Local Wind*, 234 pp., Cambridge Univ. Press, New York, 1994.

1248 Singh, A. and Kuang, C.: *Scanning Mobility Particle Sizer (SMPS) Instrument Handbook*. U.S.
1249 Department of Energy, Atmospheric Radiation Measurement user facility, Richland,
1250 Washington. DOE/SC-ARM-TR-147, 2024.

1251 Skamarock, W. C., Klemp, J. B., Dudhia, J., Gill, D. O., Barker, D., Wang, W., Powers, J. G.:
1252 A description of the Advanced Research WRF version 3. NCAR Tech. Note
1253 NCAR/TN-475+STR, 113 pp., doi:10.5065/D68S4MVH, 2008.

1254 Song, S. K., Choi, Y. N., Choi, Y., Flynn, J., & Sadeghi, B.: Characteristics of aerosol chemical
1255 components and their impacts on direct radiative forcing at urban and suburban
1256 locations in Southeast Texas. *Atmospheric Environment*, 246.
1257 <https://doi.org/10.1016/j.atmosenv.2020.118151>, 2021. Maria, V. D., Rahman, M.,
1258 Collins, P., Dondi, G., & Sangiorgi, C. (2013). Urban Heat Island Effect: Thermal
1259 Response from Different Types of Exposed Paved Surfaces. *International Journal of*
1260 *Pavement Research and Technology*, 6(4), 414-422.
1261 [https://doi.org/10.6135/ijprt.org.tw/2013.6\(4\).414](https://doi.org/10.6135/ijprt.org.tw/2013.6(4).414)

1262 Soni, M., Verma, S., Mishra, M. K., Mall, R. K., and Payra, S.: Estimation of particulate matter
1263 pollution using WRF-Chem during dust storm event over India. *Urban Climate*, 44.
1264 <https://doi.org/10.1016/j.uclim.2022.101202>, 2022.

1265 Stockwell, W. R., Middleton, P., Chang, J. S., and Tang, X.: The second generation regional
1266 acid deposition model chemical mechanism for regional air quality modeling. *Journal*
1267 *of Geophysical Research*, 95(D10), 16343–16367.
1268 <https://doi.org/10.1029/JD095iD10p16343>, 1990.

1269 Subba, T., Zhang, Y., & Steiner, A. L.: Simulating the transport and rupture of pollen in the
1270 atmosphere. *Journal of Advances in Modeling Earth Systems*, 15, e2022MS003329.
1271 <https://doi.org/10.1029/2022MS003329>, 2023.

1272 Subramanian, A., Nagarajan, A. M., Vinod, S., Chakraborty, S., Sivagami, K., Theodore, T.,
1273 Sathyanarayanan, S. S., Tamizhdurai, P., & Mangesh, V. L. (2023). Long-term impacts
1274 of climate change on coastal and transitional eco-systems in India: an overview of its
1275 current status, future projections, solutions, and policies. In *RSC Advances* (Vol. 13,
1276 Issue 18, pp. 12204–12228). Royal Society of Chemistry.
1277 <https://doi.org/10.1039/d2ra07448f>

1278 Talbot, C., Augustin, P., Leroy, C., Willart, V., Delbarre, H., Khomenko, G.: Impact of a sea
1279 breeze on the boundary-layer dynamics and the atmospheric stratification in a coastal
1280 area of the North Sea. *BoundaryLayer Meteorology*, 125, 133–154, 2007.

- 1281 Thompson, S. A., Chen, B., Matthews, B.H., Li, R., Nowotarski, C. J., Rapp, A. D., & Brooks,
1282 S. D. (2025). Characterizing Greater Houston's aerosol by air mass during TRACER.
1283 Journal of Geophysical Research: Atmospheres, 130, e2025JD043353.
1284 <https://doi.org/10.1029/2025JD043353>.
- 1285 Tuccella, P., Curci, G., Visconti, G., Bessagnet, B., Menut, L., & Park, R. J.: Modeling of gas
1286 and aerosol with WRF/Chem over Europe: Evaluation and sensitivity study. Journal of
1287 Geophysical Research Atmospheres, 117(3). <https://doi.org/10.1029/2011JD016302>,
1288 2012.
- 1289 Twomey, S.: Pollution and the planetary albedo. Atmos. Environ., 8, 1251–1256, 1974.
- 1290 Uin, J., Aiken, A. C., Dubey, M. K., Kuang, C., Pekour, M., Salwen, C., Sedlacek, A. J.,
1291 Senum, G., Smith, S., Wang, J., Watson, T. B., & Springston, S. R.: Atmospheric
1292 radiation measurement (ARM) aerosol observing systems (AOS) for surface-based in
1293 situ atmospheric aerosol and trace gas measurements. Journal of Atmospheric and
1294 Oceanic Technology, 36(12), 2429–2447. [https://doi.org/10.1175/JTECH-D-19-](https://doi.org/10.1175/JTECH-D-19-0077.1)
1295 0077.1, 2019.
- 1296 Verma, S., Boucher, O., Venkataraman, C., Reddy, M. S., Müller, D., Chazette, P., &
1297 Crouzille, B.: Aerosol lofting from sea breeze during the Indian Ocean Experiment.
1298 Journal of Geophysical Research, 111, 07208. <https://doi.org/10.1029/2005JD005953>,
1299 2006.
- 1300 Viner, B., Noble, S., Qian, J. H., Werth, D., Gayes, P., Pietrafesa, L., and Bao, S.: Frequency
1301 and characteristics of inland advecting sea breezes in the Southeast United States.
1302 Atmosphere, 12(8). <https://doi.org/10.3390/atmos12080950>, 2021.
- 1303 Wang, B., Geddes, J. A., Adams, T. J., Lind, E. S., McDonald, B. C., He, J., Harkins, C., Li,
1304 D., and Pfister, G. G.: Implications of Sea Breezes on Air Quality Monitoring in a
1305 Coastal Urban Environment: Evidence From High Resolution Modeling of NO₂ and
1306 O₃. Journal of Geophysical Research: Atmospheres, 128(11).
1307 <https://doi.org/10.1029/2022jd037860>, 2023.
- 1308 Wang, D., Jensen, M. P., Taylor, D., Kowalski, G., Hogan, M., Wittemann, B. M.,
1309 Rakotoarivony, A., Giangrande, S. E., & Park, J. M.: Linking Synoptic Patterns to
1310 Cloud Properties and Local Circulations Over Southeastern Texas. Journal of

1311 Geophysical Research: Atmospheres, 127(5). <https://doi.org/10.1029/2021JD035920>,
1312 2022.

1313 Wang, D., Melvin, E. C., Smith, N., Jensen, M. P., Gupta, S., Abdullah-Smoot, A., Pszeniczny,
1314 N., & Hahn, T.: TRACER Perspectives on Gulf-Breeze and Bay-Breeze Circulations
1315 and Coastal Convection. *Monthly Weather Review*, 152(10), 2207–2228.
1316 <https://doi.org/10.1175/MWR-D-23-0292.1>, 2024.

1317 Wang, K., Zhang, Y., Yahya, K.: Decadal application of WRF/Chem over the continental U.S.:
1318 Simulation design, sensitivity simulations, and climatological model evaluation.
1319 *Atmospheric Environment*, 253, 118331,
1320 <https://doi.org/10.1016/j.atmosenv.2021.118331>, 2021.

1321 Wang, S. C., Wang, Y., Estes, M., Lei, R., Talbot, R., Zhu, L., & Hou, P.: Transport of Central
1322 American Fire Emissions to the U.S. Gulf Coast: Climatological Pathways and Impacts
1323 on Ozone and PM_{2.5}. *Journal of Geophysical Research: Atmospheres*, 123(15), 8344–
1324 8361. <https://doi.org/10.1029/2018JD028684>, 2018.

1325 Watson, TB.: Aerosol Chemical Speciation Monitor (ACSM) Instrument Handbook. U.S.
1326 Department of Energy, Atmospheric Radiation Measurement user facility, Richland,
1327 Washington.DOE/SC-ARM-TR-196, 2024.

1328 Wert, B. P., Trainer, M., Fried, A., Ryerson, T. B., Henry, B., Potter, W., Angevine, W. M.,
1329 Atlas, E., Donnelly, S. G., Fehsenfeld, F. C., Frost, G. J., Goldan, P. D., Hansel, A.,
1330 Holloway, J. S., Hubler, G., Kuster, W. C., Nicks, D. K., Neuman, J. A., Parrish, D. D.,
1331 ... Wisthaler, A.: Signatures of terminal alkene oxidation in airborne formaldehyde
1332 measurements during TexAQ_S 2000. *Journal of Geophysical Research D:*
1333 *Atmospheres*, 108(3). <https://doi.org/10.1029/2002jd002502>, 2003.

1334 Westenbarger, D. A., & Morris, G. A.: Identifying biomass burning impacts on air quality in
1335 Southeast Texas 26–29 August 2011 using satellites, models and surface data.
1336 <https://doi.org/10.5194/acp-2017-1234>, 2018.

1337 Yoon, S., Ortiz, S. M., Clark, A. E., Barrett, T. E., Usenko, S., Duvall, R. M., Ruiz, L. H.,
1338 Bean, J. K., Faxon, C. B., Flynn, J. H., Lefer, B. L., Leong, Y. J., Griffin, R. J., &
1339 Sheesley, R. J.: Apportioned primary and secondary organic aerosol during pollution
1340 events of DISCOVER-AQ Houston. *Atmospheric Environment*, 244.
1341 <https://doi.org/10.1016/j.atmosenv.2020.117954>, 2021.

1342

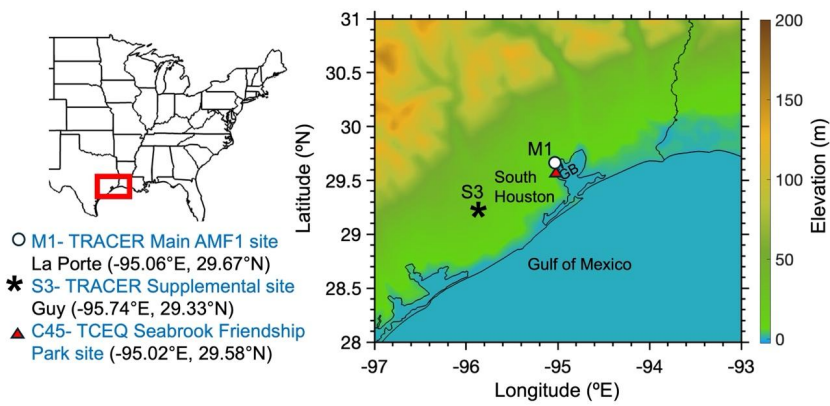
1343

1344

1345

1346

1347



1348

1349 **Figure 1.** Map showing the TRACER field campaign main site (M1) and supplemental site
1350 (S3), and the TCEQ Seabrook Friendship Park site (C45). Terrain elevation is shown in color.
1351 Here, “GB” corresponds to the Galveston Bay.

1352

1353

1354

1355

1356

1357

1358

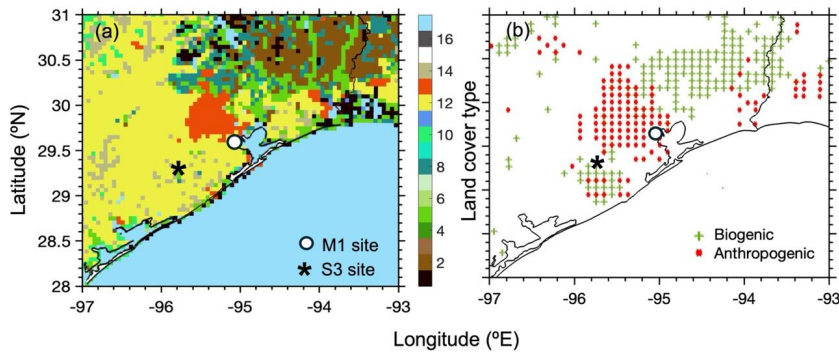
1359

1360

1361

1362

1363
1364
1365
1366



1367

1368 **Figure 2.** Weather Research and Forecasting model coupled with Chemistry (WRF-Chem)
1369 simulation domain with (a) primary land cover types comprising of (1) Evergreen Needleleaf
1370 Forest, (2) Evergreen Broadleaf Forest, (3) Deciduous Needleleaf Forest, (4) Deciduous
1371 Broadleaf Forest, (5) Mixed Forest, (6) Closed Shrubland, (7) Open Shrubland, (8) Woody
1372 Savanna, (9) Savanna, (10) Grassland, (11) Permanent Wetlands, (12) Cropland, (13) Urban
1373 and Build-up, (14) Cropland/Natural Mosaic, (15) Snow and Ice, (16) Barren or Sparsely
1374 Vegetated, and (17) Water; (b) Anthropogenic (red dots) and biogenic (green dots) aerosol
1375 emission source points obtained using the National Emissions Inventory (NEI) data and Model
1376 of Emissions of Gases and Aerosols from Nature (MEGAN) modeling system, respectively.

1377

1378

1379

1380

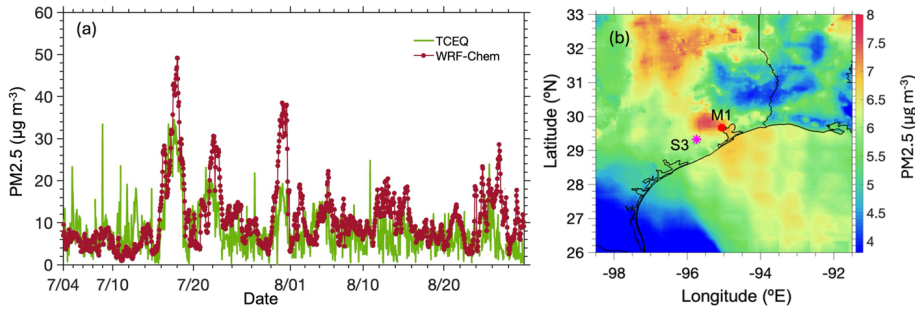
1381

1382

1383

1384

1385



1386

1387 **Figure 3.** (a) Comparison of daily averaged $PM_{2.5}$ observed (green) at the TCEQ site, and

1388 WRF-Chem simulated (red) at the M1 site. (b) Spatial distribution of WRF-Chem simulated

1389 August 2022 mean $PM_{2.5}$ (filled contours).

1390

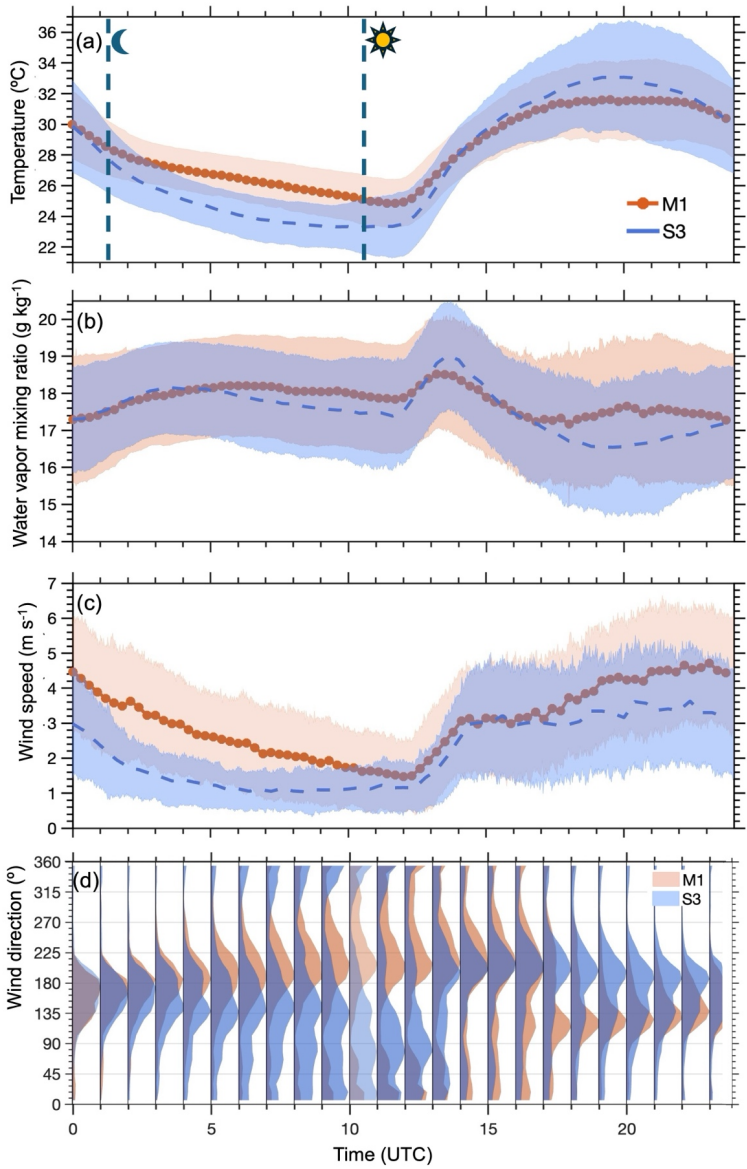
1391

1392

1393

1394

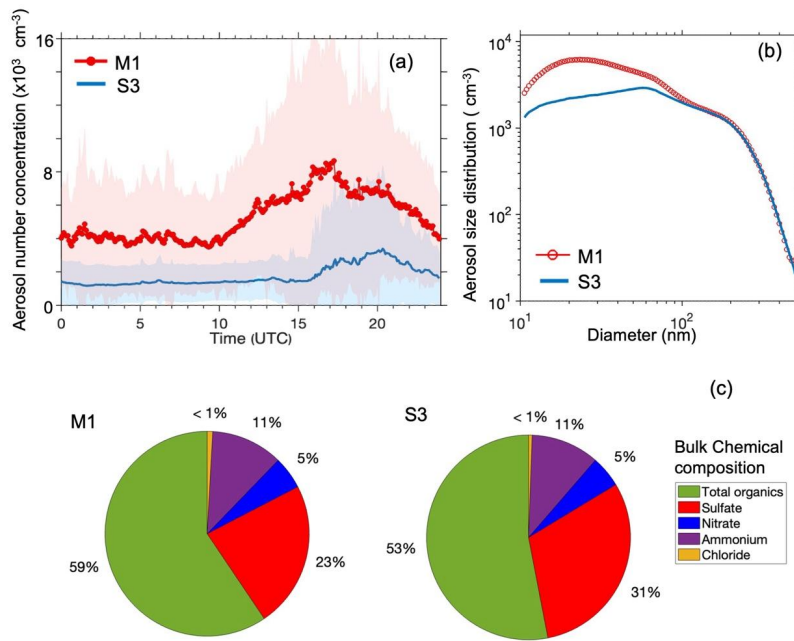
Deleted: Spatial distribution of averaged $PM_{2.5}$ simulated with WRF-chem (color-filled contour)



1397

1398 **Figure 4.** Diurnal variation of meteorological variables (a) Temperature at 2 m, (b) water vapor
 1399 mixing ratio (w) (c) wind speed at 10 m, and (d) wind direction waterfall diagram at 10 m
 1400 measured at M1 (in orange) and S3 (in blue) sites averaged during IOP. The shaded color
 1401 represents the standard deviation from the mean.

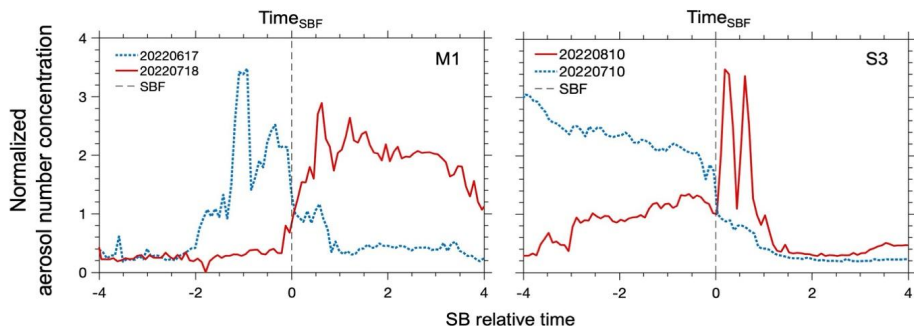
1402
1403
1404



1405
1406
1407
1408
1409
1410
1411
1412
1413
1414

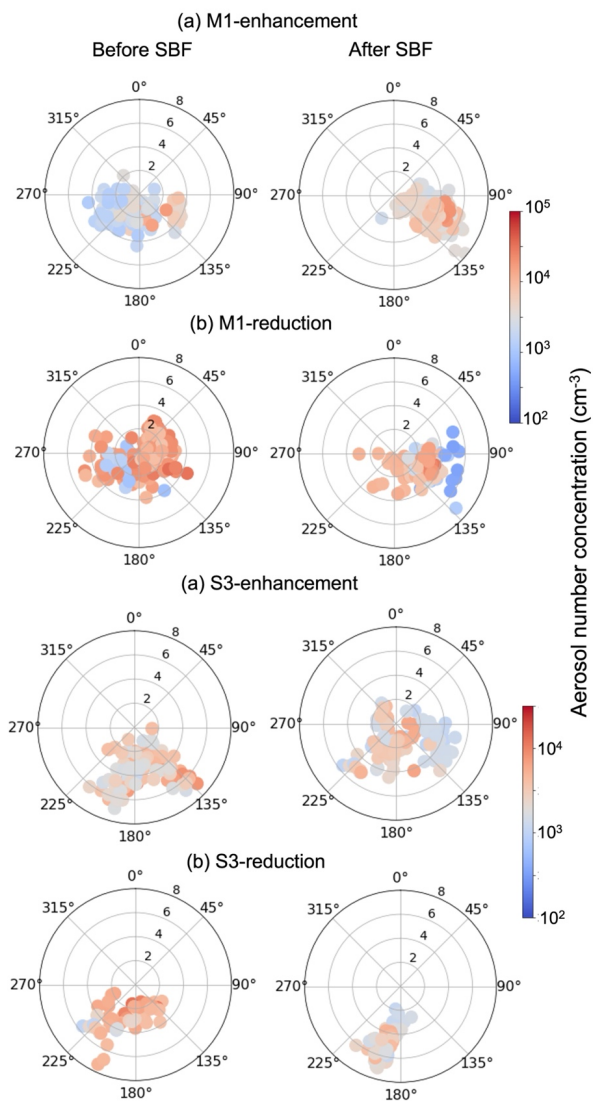
Figure 5. Measured (a) diurnal distribution of aerosol number concentration, (b) aerosol size distribution, and (c) percentage contribution of bulk chemical composition at M1 and S3 sites averaged from June to September 2022.

1415
1416
1417
1418



1419
1420
1421
1422
1423

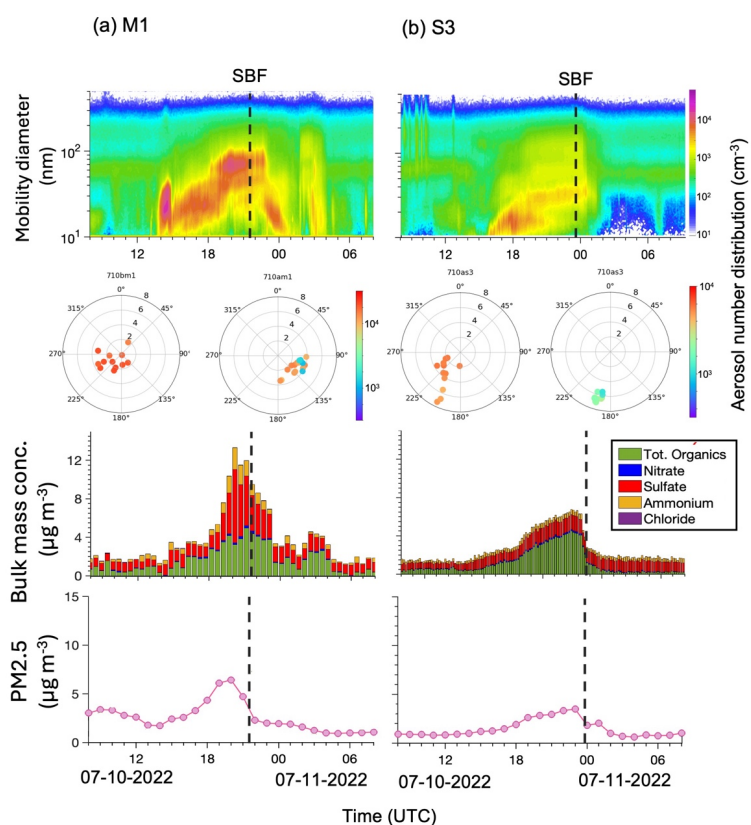
Figure 6. Time series of the normalized aerosol number concentration, with the time centered at the time of the passing of the SBF ($T_{\text{SBF}}=0$) at the M1 site (1st column) and the S3 site (2nd column) during the individual SB event days.



1424

1425 **Figure 7.** Open-air polar plots for aerosol number concentration before and after the passing
 1426 of the SBF ($\Delta T = T_{\text{SBF}} \pm 1$) during (a) enhancement and (b) reduction events at M1 and S3 sites.
 1427 The wind speed (in m s^{-1}) grid lines are presented with black circles; the color scales represent
 1428 the concentrations observed with each wind speed and direction combinations.

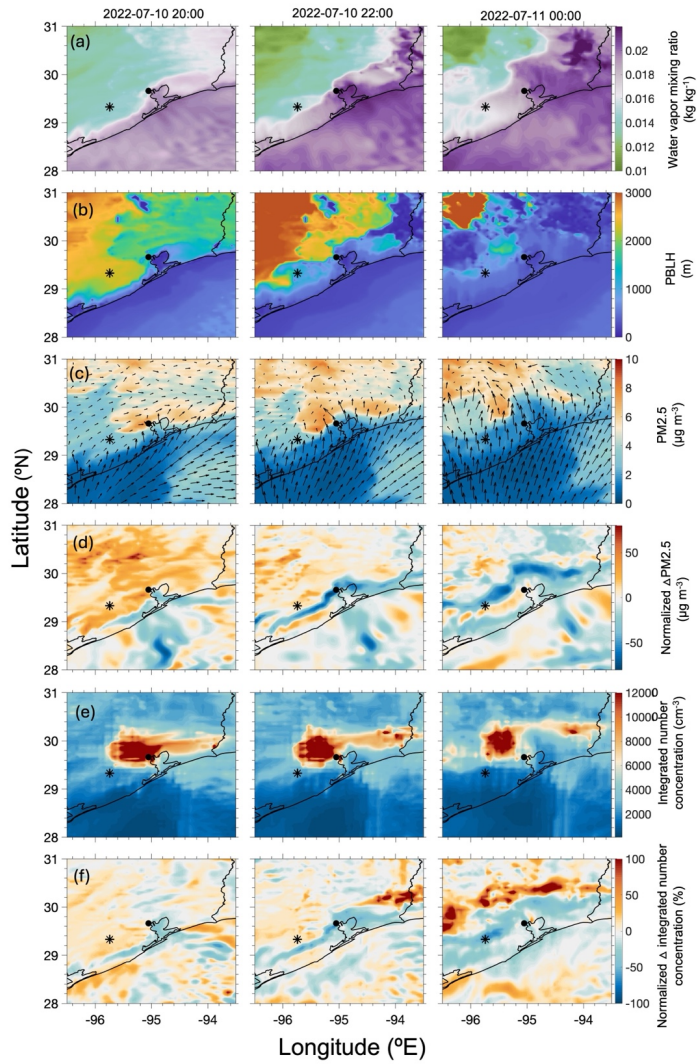
1429
1430
1431
1432



1433

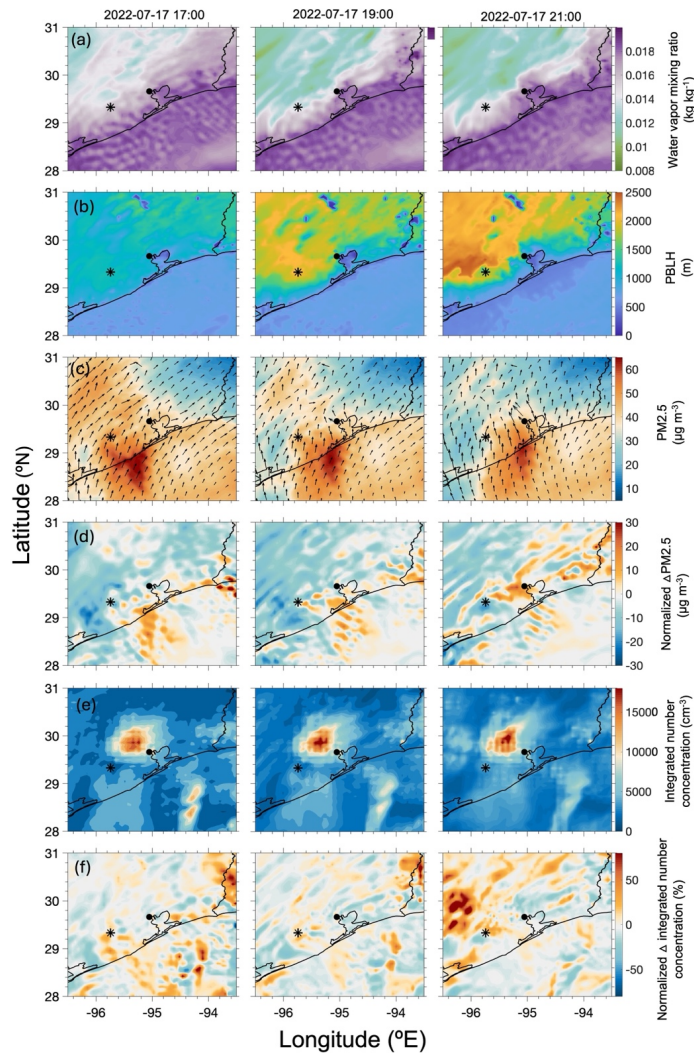
1434 **Figure 8.** Time series of measured aerosol size distribution (1st row), measured bulk chemical
1435 composition (3rd row), and modeled $\text{PM}_{2.5}$ mass concentration (4th row) at (a) M1 and (b) S3
1436 on 10 July 2022. Polar plot showing the measured integrated aerosol number concentration
1437 during one hour before and after the passing of the SBF (2nd row). The black dashed line
1438 represents the time of the passing of the SBF (T_{SBF}) at the respective sites.

Deleted: and TCEQ measured



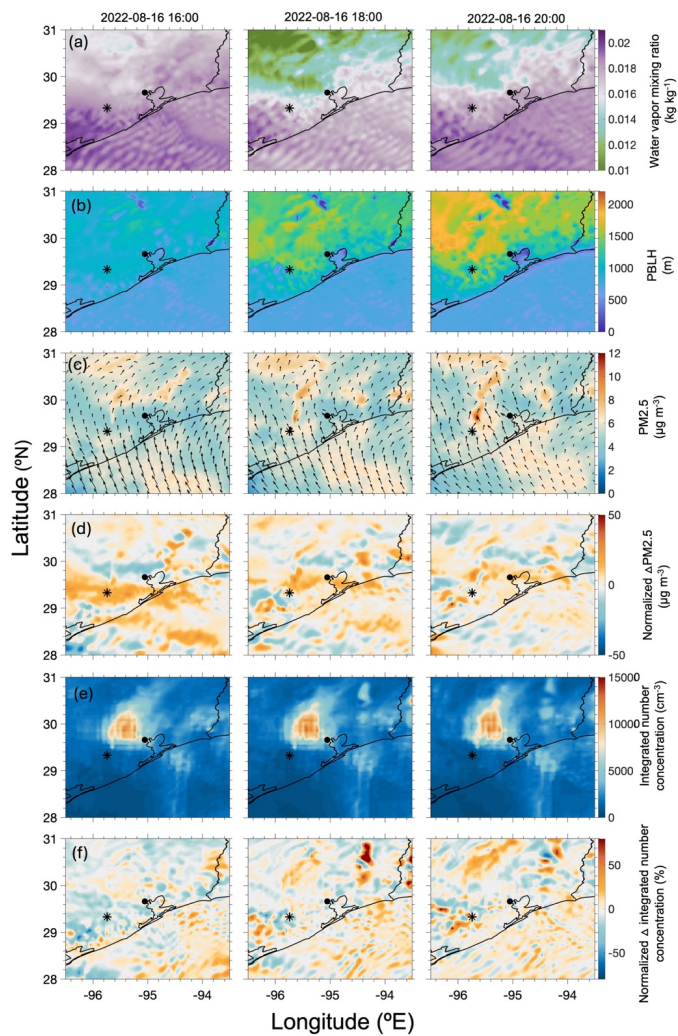
1440

1441 **Figure 9.** Modeled surface distribution of (a) water vapor mixing ratio (w), (b) PBLH, (c)
 1442 $PM_{2.5}$, and wind vector (black arrows, at the surface), and (e) integrated aerosol number
 1443 concentration (nucleation + accumulation mode) at three-time steps: 20:00 and 22:00 UTC on
 1444 10 July, and 00:00 UTC on 11 July. Sub-panels (d) and (f) show the normalized changes, where
 1445 Δ is the change from the previous time step. The filled-circle marker in the panels represent the
 1446 M1 site, while the star represents the S3 site.



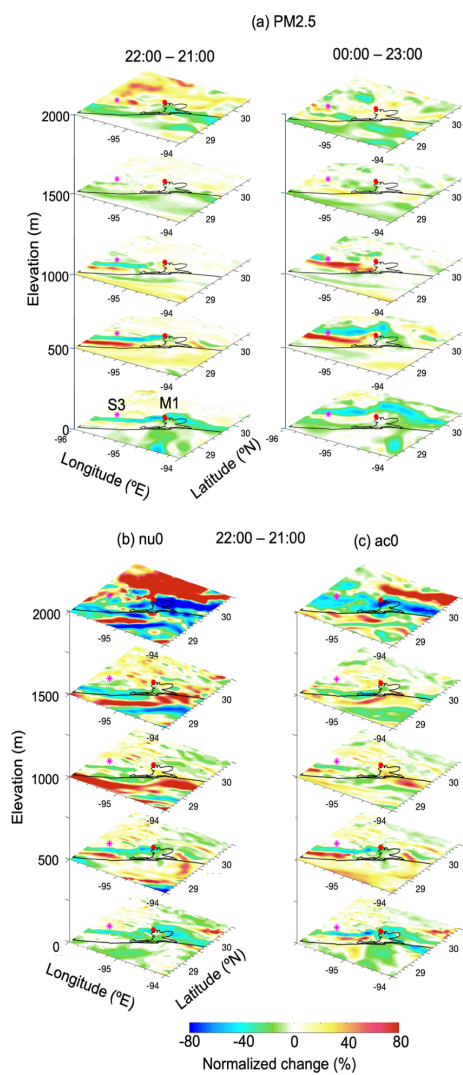
1447

1448 **Figure 10.** Modeled surface distribution of (a) water vapor mixing ratio (w), (b) PBLH, (c)
 1449 $PM_{2.5}$, and wind vector (black arrows, at the surface), and (e) integrated aerosol number
 1450 concentration (nucleation + accumulation mode) at three-time steps: 17:00, 19:00 and 21:00
 1451 UTC on 17 July. Sub-panels (d) and (f) show the normalized changes, where Δ is the change
 1452 from the previous time step. The filled-circle marker in the panels represent the M1 site, while
 1453 the star represents the S3 site.



1454

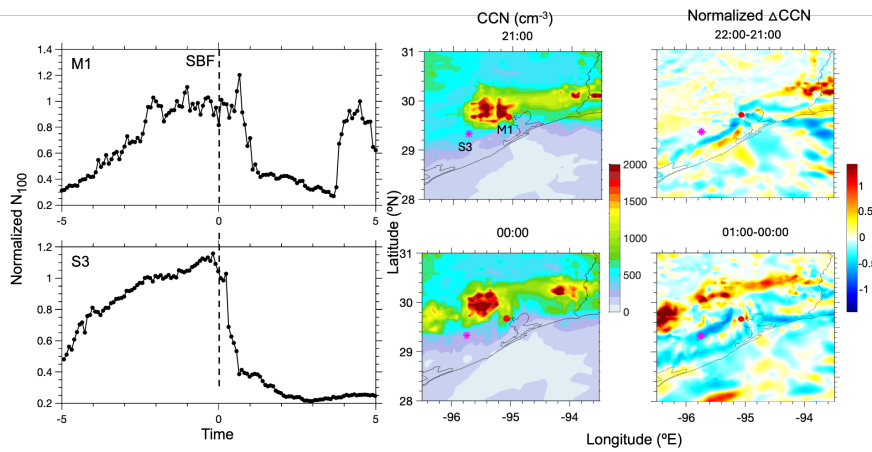
1455 **Figure 11.** Modeled surface distribution of (a) water vapor mixing ratio (w), (b) PBLH, (c)
 1456 $PM_{2.5}$, and wind vector (black arrows, at the surface), and (e) integrated aerosol number
 1457 concentration (nucleation + accumulation mode) at three-time steps: 16:00, 18:00 and 20:00
 1458 UTC on 16 August. Sub-panels (d) and (f) show the normalized changes, where Δ is the change
 1459 from the previous time step. The filled-circle marker in the panels represent the M1 site, while
 1460 the star represents the S3 site.



1462

1463 **Figure 12.** First row: the spatial distribution of normalized $\Delta PM_{2.5}$ at different elevations at
 1464 timesteps (a) 21:00 and 22:00 UTC on 10 July, and 23:00 UTC on 10 July and 00:00 UTC on
 1465 11 July. Second row: the spatial distribution of normalized (b) Δ nucleation mode (nu0) and (c)
 1466 Δ accumulation mode (ac0) aerosol number concentration at timesteps 21:00 and 22:00 UTC
 1467 on 10 July.

1468
1469
1470
1471
1472
1473
1474



1475

1476 **Figure 13.** Time series of the normalized measured N_{100} along the time of the SBF's passing
1477 through the M1 site (first row) and the S3 site (second row) on 10 July 2022 (1st column).
1478 Spatial distribution of the modeled hourly averaged (2nd column) and normalized ΔCCN (3rd
1479 column).

1480

1481

1482

1483

1484

1485

1486

1487 **Table 1:** Summary of SBC influence on aerosol number concentration at the M1 and S3 sites.
1488 Events are classified into enhancement, reduction, and neutral categories.

1489

Site	Description	Combined	Enhancement	Reduction	Neutral
M1	Days (fraction of the total events %)	46 (total SB events)	13 (28 %)	16 (35 %)	17 (37 %)
	Concentration change (after - before) %	-23 (all enhancement + reduction events)	+55	-42	-11
		-7 (total number of events)			
S3	Days	30 (total SB events)	8 (27 %)	4 (13 %)	18 (60 %)
	Concentration change (after - before) %	+9 (all enhancement + reduction events)	+64	-45	-10
		+3 (total number of events)			

1490

1491

1492

1493

1494

1495

1496

1497

1498

1499

1500

1501 **Table 2.** Model configuration

Simulation period	1 July - 30 August 2022
Domain	26 to 33 °N and -98 to -92 °E
Horizontal resolution (dx)	5 x 5 km
Vertical resolution	45 layers from 1000-50 mb
Meteorological initial and boundary conditions	North America mesoscale (NAM) forecast output at T221 (32-km) resolution, 28 vertical levels (Bauman, 2010)
Shortwave radiation	Goddard shortwave radiation scheme (Chou et al., 1998)
Longwave radiation	The rapid radiative transfer mode (RRTM) (Mlawer et al., 1997)
Land surface	Community National Center for Environmental Prediction (NCEP), Oregon State University, Air Force, and Hydrologic Research Lab-NWS Land Surface Model (NOAH) (Chen and Dudhia, 2001)
Surface Layer	Monin-Obukhov (Monin and Obukhov, 1954; Janjic, 2002)
PBL	Yonsei University Scheme (YSU) (Hong et al., 2006)
Cumulus	The Grell scheme (Grell and Devenyi 2002)
Microphysics	Morrison 2-moment scheme (Morrison, 2005)
Chemical mechanism	RACM Chemistry with MADE/VBS aerosols using KPP library along with the volatility basis set (VBS) used for Secondary Organic Aerosols (Stockwell et al., 1990; Ackerman et al., 1998; Schell et al., 2001)
Chemical initial and boundary conditions	MOZBC from the Model for Ozone and Related chemical Tracers (MOZART) model (Emmons et al., 2010)
Anthropogenic emissions	National Emissions Inventory (NEI), U.S. Environmental Protection Agency (EPA)
Biogenic emissions	The Model of Emissions of Gases and Aerosols from Nature version MEGAN v2.1 biogenic emissions (Guenther et al., 2012)

1502